Characterization of the ALPIDE chip with Helium-4 ions for Proton Computed Tomography

A thesis by

Simon Kristian Huiberts

for the degree of

Master of Science in Physics

Department of Physics and Technology

University of Bergen

November 2018

Abstract

Particle therapy has become an appealing therapeutic option for patients with various tumor types. The physical properties of charged particles allow for an improved dose distribution conformality compared to conventional photon-based radiotherapy. This advantage translates into a reduction of unwanted side effects from radiation treatment and in the long run will improve the patient's quality of life. A team at the University of Bergen is developing a proton Computed Tomography (pCT) scanner prototype. This technology will primarily work as a supplement to particle therapy as it aims to enhance the accuracy of the pre-calculated dose plans applied during treatment.

The pCT system is a Digital Tracking Calorimeter (DTC) consisting of multiple layers of the ALPIDE CMOS Monolithic Active Pixel Sensor with the aim of tracking protons and measure its energy. This thesis studies the ALPIDE chip towards its medical applications in the future DTC. It will describe the clusters created on the chip by helium ions and alpha particles with a focus on the parameters that affect the pixel size of the clusters.

Results from an analysis of a helium microbeam indicate that the size of a cluster correlates with the position of the incoming particle on the pixel and hence, the interior location of the energy deposition. These clusters varied in size from 5 to 35 pixels when the beam scanned the chip in μm steps. Moreover, an experiment conducted during this project shows that the size of the clusters is dependent on the temperature of the chip and that the average size of the cluster gets larger with increasing temperature. In the end, the results obtained from an ALPIDE telescope irradiated with high energetic helium beams is described. This experiment shows that the clusters used in tracking increases in size at higher Linear Energy Transfer (LET) of the particles.

Preface

The two main experiments outlined in this thesis were conducted at the Australian Nuclear Science and Technology Organisation (ANSTO) microbeam facility in January 2018 and the Heidelberg Ion-Beam Therapy Center (HIT) in July 2018. The analysis of the data was carried out at the Department of Physics and Technology at the University of Bergen between January and November 2018.

Acknowledgments

I am grateful for the opportunity I was granted to be able to work closely with the team involved in the pCT project. My supervisor Professor Dieter Röhrich encouraged me to pursue the tasks in the project that interested me the most and this freedom has motivated me throughout my work. Thanks to Dieter Röhrich for your guidance and the valuable advice I got along the way.

A warm thanks to Ganesh Tambave for your time devoting to helping me overcome the problems I faced along the way. Thank you for your help and support. A huge thanks to Pierluigi Piersimoni, Andreas Samnøy, Ola Grøttvik and Helge Pettersen for the support I got towards practical and theoretical purposes and for the effort put into answering the questions I brought up along the way. I would also like to thank Monika Varga-Kofarago, Lennart Volz, Sudar Akos and Qasim Malik for the discussions and help regarding the project.

Thanks to my fellow students at room 534. It has been fun working with you, and I hope all the best for you in the future. Special thanks to Viljar Eikland and Susmita Afroz for the teamwork and Ingrid Lofnes for our helpful discussions.

Finally, I would like to thank my friends for providing me with encouragement and support. A special thanks to my family and my beloved Hilde Haugland for showing an interest in the achievements along the way, as well as all the support I got at difficult times. Thank you for enduring everything and for always being there.

Simon Kristian Huiberts
Bergen, November 2018

Contents

List of Figures

CHAPTER 1

Introduction

1.1 Background and Motivation

Cancer is a destructive disease involving abnormal cell growth, halting organ function and damaging the body's healthy tissue. Radiation therapy can treat many types of cancer by eliminating the tumor entirely or by relieving the cancer symptoms.

In 2017, more than 174 000 patients were treated with charged particles worldwide. The benefits of particle therapy over X-ray photon therapy is the maximization of the delivered dose ratio between the tumor and healthy tissue, sparing healthy organs surrounding the tumor. This advantage reduces the unwanted side effects connected with radiation treatment and in the long run, improves the patient's quality of life. In 2018 it was finally decided to establish two proton therapy centers in Norway, which are expected to be operational from 2023 and 2025 in Oslo and Bergen, respectively.

As of today, the patient's dose distribution plan for protons is based on Hounsfield maps obtained by conventional X-ray CT scans. These values, however, has to be calibrated into Stopping Power, and this conversion introduces range uncertainties in the proton treatment planning. The range uncertainties can be reduced in proton Computed Tomography (pCT) by measuring the stopping power directly, excluding the need for an inconvenient converting step. In succeeding building a clinical working pCT prototype, the accuracy of the proton treatment enhances and thus leading to better particle treatment in the future.

1.2 About this Thesis

The primary goal of this thesis is to characterize the ALPIDE chip towards its medical application in the future proton CT prototype, developed at the University of Bergen. The aim is to use the ALPIDE chips as the Digital Tracking Calorimeter (DTC)

for tracking and measure the initial energy of the protons. The clusters created in the chip by the transverting particle plays an essential role for these purposes. The center of gravity of these clusters are used as tracking hits, and their size is utilized to measure the deposited energy in each layer. This thesis focuses on the parameters connected to the size of the clusters produced in the ALPIDE chip.

Much time went into analyzing the data collected at the ANSTO facility. The results from this experiment were obtained by writing code in c++ and ROOT to process and plot the data. Time was spent working together with the pCT group to plan and conduct the experiment at the HIT facility, and to make the Data Acquisition (DAQ) software and the analysis software work. Some time was spent conducting other smaller experiments at the University of Bergen, and to design the ALPIDE telescope stand.

1.3 Thesis Outline

This thesis is divided into the following chapters:

Chapter 2: Radiation and its medical purposes This chapter starts with describing theory regarding radiation and interaction of photons and charged particles. This theory is required to understand the benefits of proton beam radiotherapy over conventional photon therapy. The chapter follows with an explanation of the differences between conventional X-ray CT and proton CT. It ends with a discussion on the proton CT prototype development at the University of Bergen.

Chapter 3: Silicon Pixel Detectors This chapter describes silicon semiconductors with emphasize on electron-hole pair generation and the transportation of these charge carriers in the silicon. After that, theory around pixels and especially Monolithic Active Pixel Sensors (MAPS) is presented. The chapter ends with a description of clusters created on CMOS MAPS structures.

Chapter 4: The ALPIDE chip This chapter aims to describe the fundamentals of the ALPIDE chip with an emphasis on the readout electronics. The trigger and strobe mechanisms are described, followed by examples of how a charge signal can be read out twice into two consecutive strobes. Finally, the ALPIDE's function in the pCT is outlined, with a focus on how the clusters are utilized to estimate the energy deposition in each layer.

Chapter 5: Characterization of the ALPIDE This chapter begins with the experiment conducted at the Univerity of Bergen on cluster development. It follows by a detailed analysis of the ANSTO microbeam experiment, explaining the position vs. clusters size dependency that was observed. After that, the induced radiation damage effects from the helium microbeam is discussed. It ends with a presentation of a second experiment conducted at the University of Bergen concerning the cluster size variations at different temperatures of the chip.

Chapter 6: Characterization of the ALPIDE Telescope This chapter starts with presenting the experiment conducted at the Heldeberg ion-Beam therapy center. The experimental setup, as well as the beam parameters, are outlined here together with a brief discussion on the software used for data acquisition and analysis. Finally, the results obtained regarding the cluster sizes at different helium energies are presented.

Chapter 7: Discussion and conclusion This chapter summarizes the results presented in this thesis, as well as a discussion on its relevance for the pCT development. It ends with suggestions on further work in this field.

1.4 Citation Principles

The citations used in this thesis which are listed before the ending punctuation of a paragraph refers to multiple statements in the section. Citations listed in a sentence in the paragraph refers to the statement itself.

CHAPTER 2

Radiation and its application in medicine

This chapter outlines a basic description of how electromagnetic radiation and charged particles interact with matter. Further, an explanation of radiotherapy is provided, together with a discussion on the advantages of particle treatment over conventional photon therapy. In the end, a description of proton computed tomography, and its benefits in medical imaging are provided.

2.1 Radiation

Radiation is energy propagating through space or an intervening medium in the form of electromagnetic waves or particles. It is often characterized as either ionizing radiation or non-ionizing radiation. Ionizing radiation can ionize the medium it passes through by kicking out an orbiting electron from the atomic shell. This happens either directly or indirectly depending on the mechanism behind the interaction. Directly ionizing radiation occurs if the particle is a charge carrier, such as an alpha particle or an electron, with sufficient energy to ionize the atom without any intermediate steps (i.e., directly) through the Coulomb force. For a non-charged particle such as a photon or a neutron, this ionization process happens in two phases. First, the uncharged particle deposits energy to the medium releasing a charged particle, then the charged particle deposits energy through direct Coulomb interactions. In non-ionizing radiation, the electromagnetic wave does not have enough energy for any of the ionization processes to occur [1].

2.2 Interaction of photons with matter

Photons are elementary particles described as a quantum of the electromagnetic field. It has zero mass, no electric charge and its energy is proportional to its wave frequency.

Photons are frequently used in diagnostic imaging and conventional radiotherapy. In order to understand how photons are utilized for medical purposes, one has to look at the fundamental interactions of photons with matter [1].

When a mono-energetic photon beam is traversing through a medium, its intensity will decrease exponentially. The reduction of intensity after a traveled distance x in the medium is given by:

$$I(x) = I(0)e^{-\mu x}, \tag{2.1}$$

where $I(0)$ is the initial intensity of the beam and μ is the linear attenuation coefficient. This coefficient is dependent on the atomic number Z of the material and also on the energy hv of the photon.

The attenuation of the beam is due to the photon interactions inside the medium. The photon will interact with matter mainly via three processes:

i) Photoelectric effect

ii) Compton scattering

iii) Pair production

These interactions lead to only two possible outcomes for the photon; either the photon gets completely absorbed (photoelectric effect, pair production), or the photon is scattered (Compton scattering). The total cross section is found by adding the fundamental processes together, as shown in 2.1.

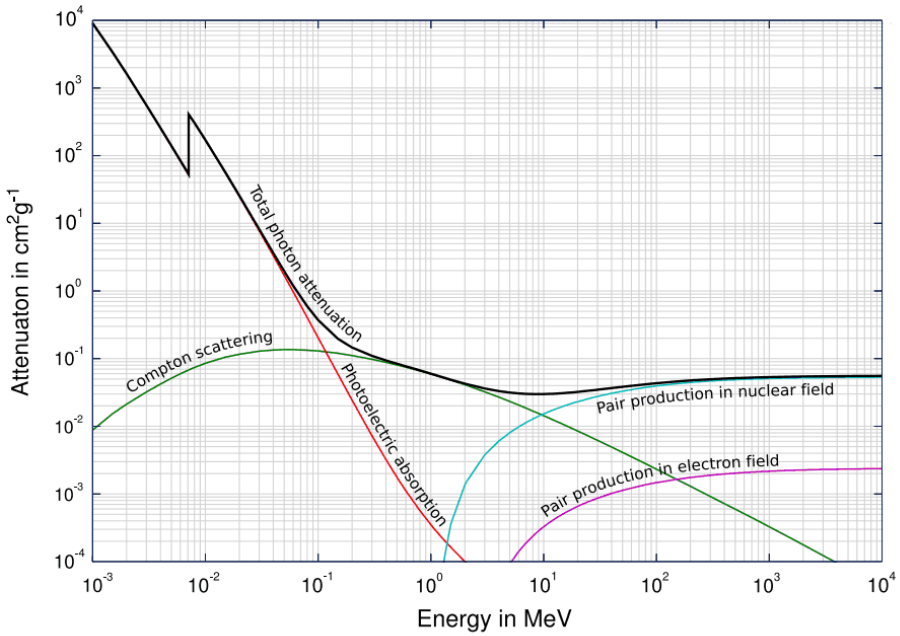

Figure 2.1: Total photon attenuation for the fundamental interactions as a function of energy in MeV [2].

This figure also shows that the interactions switch in being the dominant energy loss at different photon energies.

2.2.1 Photoelectric absorption

Photoelectric absorption, or photoelectric effect, is a process where a low energy photon gets absorbed by an electron in an atomic shell. All the photon's energy transferred to the atomic shell causes the electron to be ejected out from its orbit, as shown in figure 2.2. The interaction is most likely to occur when the electron is in the K-shell of the atom and when the photon's energy is equal to or just higher than the binding energy of the electron. This likelihood increase of the interaction can be seen in the total cross-section plot in figure 2.1 as the spike occurring on the photoelectric absorption line (red line) [1].

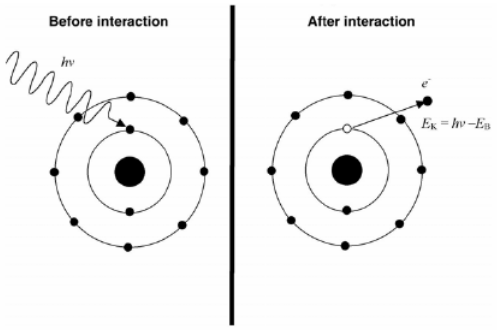

Figure 2.2: Schematic diagram of the photoelectric effect. The K-shell electron absorbs the incident photon and is ejected from its orbit with the remaining kinetic energy E_k [1].

Since the energy and momentum are conserved, the kinetic energy E_k of the ejected photoelectron is equal to the incident photon energy hv, minus the binding energy E_B of the orbital electron:

$$E_k = hv - E_B, \tag{2.2}$$

The photoelectric effect is the dominant process for low energetic photons (below 100 KeV for silicon), and the cross section is strongly dependent on the atomic number Z of the absorbing material [3]:

$$\sigma_{Photo} \propto Z^n, \tag{2.3}$$

with n varying between 4 and 5 depending on the photons' energy.

This interaction explains the intensity loss of a photon beam traversing through matter, as the photons will gradually get absorbed by atoms via the photoelectric effect [1].

2.2.2 Compton scattering

Compton scattering happens when a photon elastically scatters with a free or a loosely bound electron, as illustrated in figure 2.3. The photon transfers energy to the electron and undergoes a Compton shift (wavelength increases). The electron's momentum will increase after the collision and may cause further ionization of the medium [1].

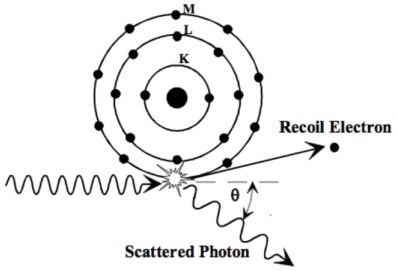

Figure 2.3: Schematic representation of the Compton effect. The incident photon scatters with a loosely bound electron. The scattering angle θ determines the amount of the photon's energy transferred to the electron [4] .

The energy of the scattered photon hv' is given by:

$$hv' = \frac{hv}{1 + \epsilon(1 - \cos\theta)}, \tag{2.4}$$

where θ is the angle between the direction of the incident photon and outgoing direction of the scattered photon. And $\epsilon = \frac{hv}{m_e c^2}$ represents the incident photon energy hv normalized to the electron rest energy $m_e c^2$.

From this formula one can observe that the energy transfer is highest when the scattered angle θ is 180° (backscattering event):

$$hv'(\theta = \pi) = \frac{hv}{1 + 2\epsilon}. \tag{2.5}$$

This process is only linearly dependent on Z. The Compton effect is the dominant process for both diagnostic and therapeutic irradiation purposes as the photon energies used here are in the range from 30 keV to 30 MeV [1].

2.2.3 Pair production

Pair production is the transformation of an energetic photon into an electron-positron pair and can happen when the photon is in the vicinity of an atomic nucleus, as shown in figure 2.4. The radiant energy converts to mass in accordance with Einstein's famous equation $E = mc^2$. This implies that the minimum energy of the photon must be at least 1022 keV (two electron masses) in order for the process to be possible. This can also be observed in the total cross-section plot as the pair production line in nuclear fields (blue line) starts at 1022 keV [1].

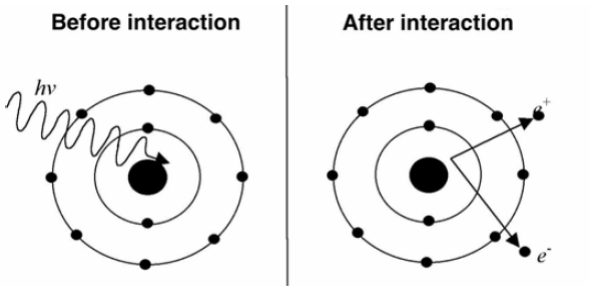

Figure 2.4: Schematic diagram of pair production. The photon is completely absorbed in the Coulomb field of the nucleus and an electron-positron pair is produced [1].

The excess energy of the photon is converted to the kinetic energy of the electron and positron. The electron and the positron can then ionize the matter directly, and the positron often annihilates with another orbital electron producing two new photons. The cross section of pair production is also dependent on the Z value of the material:

$$\sigma_{Pair} \propto Z^2, \tag{2.6}$$

and is the dominant process at energies exceeding 10 MeV [3].

2.3 Interaction of charged particles with matter

Charged particles can directly ionize the medium it penetrates. These particles have a Coulomb field that interacts with all the orbital electrons and nuclei along its trajectory. In order for a charged particle to lose all its kinetic energy, it often has to undergo a large number of collisions since each energy transfer is small. The different interactions for a charged particle traversing matter are [1]:

i) Elastic collision with the atomic electrons or with nuclei

ii) Inelastic collisions with valence electrons or nuclei

iii) Bremsstrahlung radiation

iv) Cherenkov radiation

v) Transition radiation

The most interesting interactions for ion therapy and proton imaging are elastic and inelastic collision.

2.3.1 Elastic collision

The charged particle can interact elastically with the atomic nuclei or with the orbital electrons. Depending on the polarity of the incoming charged particle, the Coulomb force that the particle experiences can either be attractive or repulsive. This process results in a deflection of the incoming particle leading to a curved path through the medium, as illustrated in figure 2.5. If the medium is thick, this will lead to multiple Coulomb scattering [1].

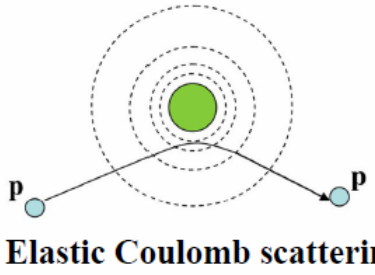

Figure 2.5: Example of an elastic collision in which a proton scatters elastically with an atomic nucleus [5].

2.3.2 Inelastic collision

Inelastic collisions with the valence electrons are the primary process in which a charged particle loses energy to the traversing medium. With high enough kinetic energy, the particle will undergo a large number of these collisions and continuously lose energy throughout its path. An example of an inelastic collision is illustrated in figure 2.6, in which a proton collides with an orbital electron [5].

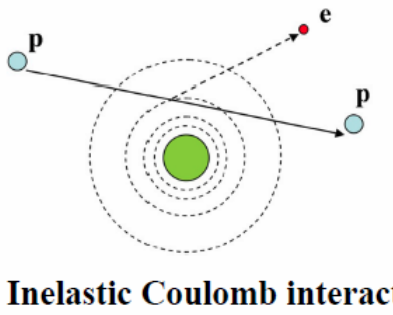

Figure 2.6: Example of a proton that ionizes an atom through inelastic collision [5].

The charged particle can also lose energy via other interactions such as Bremsstrahlung radiation, Cerenkov radiation, and Transition radiation, but the dominant energy loss process for heavy particles is by inelastic collision as mentioned above.

2.3.3 The Bethe equation

The energy loss of a charged particle along its trajectory is described with the Bethe (Bethe-bloch) equation. It is a model based on the scattering interactions that the particle has with atomic electrons in terms of the linear energy loss [3]:

$$-\left\langle \frac{dE}{dx} \right\rangle = Kz^2 \frac{Z}{A} \frac{1}{\beta^2} \left(\frac{1}{2} ln \frac{2m_e c^2 \beta^2 \gamma^2 T_{max}}{I^2} - \beta^2 - \frac{\delta(\beta\gamma)}{2} \right), \tag{2.7}$$

with

$\frac{dE}{dx}$	energy loss of the particle usually given in $\frac{\text{eV}}{\text{g/cm}^2}$
K	$4\pi N_{Av} r_e^2 m_e c^2 = 0.307075$ MeV cm^2
z	charge of the traversing particle in units of the electron charge
Z	atomic number of the absorbing medium
A	atomic mass of the absorbing medium
$m_e c^2$	rest energy of the electron (0.511 MeV)
β	velocity of the traversing particle in units of the speed of light
γ	Lorentz factor $1/\sqrt{1-\beta^2}$
I	mean excitation energy (137 eV for silicon)
T_{max}	maximum energy transfer in a single collision
$\delta(\beta\gamma)$	density effect correction to ionization loss

This particular formula is used for particles more massive than electrons, and one must apply an alternate version in order to describe the energy loss for electrons and positrons. The Bethe equations show that the energy loss is also dependent of the Z/A value of the medium and in radiation protection, often heavier elements are used (like lead or tungsten) in order to stop the particles more effectively.

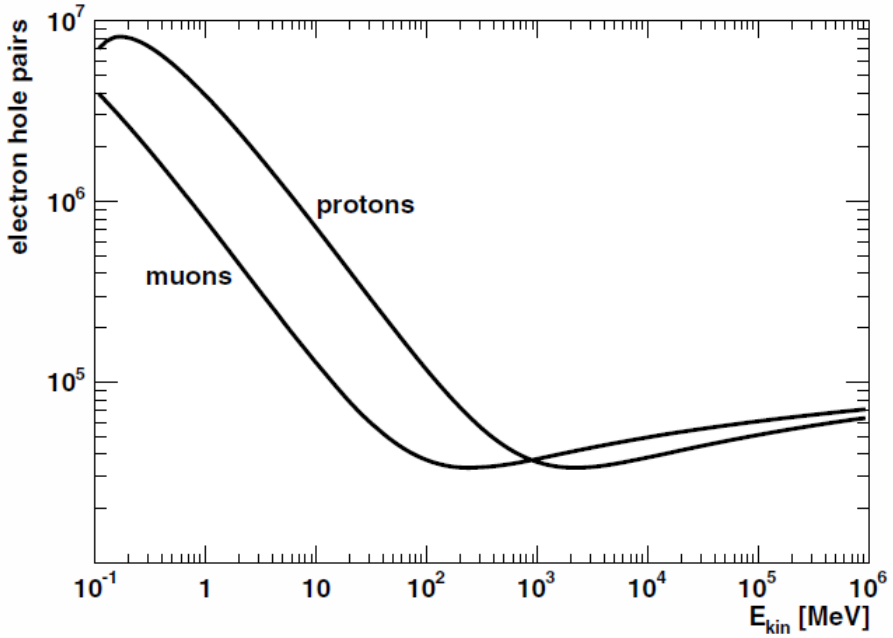

Figure 2.7: The number of electron-hole pairs generated in a 300 μm thick silicon layer for mouns and protons [3].

The linear energy loss (often referred to as the stopping power) is strongly dependent on the velocity and charge of the particle. It can be seen in figure 2.7, that the energy loss will increase as the velocity of the particle decreases. This is an essential characteristic of the charged particles, and it occurs because the mean interactions length gets shorter as the particle's velocity decreases. This leads to the Bragg peak, referred to as a small area in which the charged particles deposits all its remaining energy. As seen in figure 2.7, the graph reaches a minimum ionization point, and with this specific velocity, the particle is often referred to as a MIP (Minimum Ionization particle). Above this point, the energy loss increases gradually with higher velocities due to the relativistic effects which expands the Coulomb field of the particle [3].

2.3.4 The Bragg Curve

The Bragg curve shows the energy loss of a particle as a function of its remaining energy or depth. The charged particle gradually loses its energy and velocity when transversing through matter, and this leads to a peak (Bragg peak) in which the specific energy loss is at its maximum. The particle will then deposit a large amount of its remaining energy in a small area before it stops completely. Figure 2.8 shows the peak for a single alpha particle reaching a maximum ionization point at around 1 MeV. For a beam, however, since the energy loss of ions is a stochastic process, this

peak would have a Gaussian shaped form. After the peak, the energy deposition falls quickly and hence its ionization potential [3].

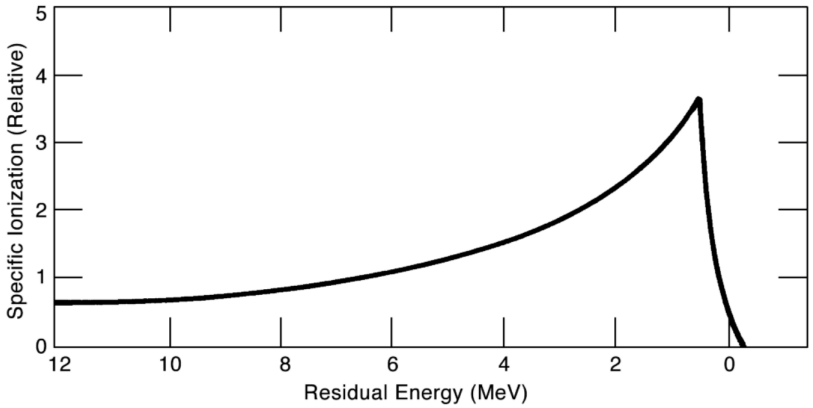

Figure 2.8: The Bragg Curve, illustrating specific ionization for an alpha particle [6].

This peak can be utilized in particle radiotherapy to deliver a large dose to the tumor location as well as minimizing the dose delivered outside this region. Also, applying several beams with energy variations leads to a spread out Bragg peak. This method is often used in radiation therapy to create a field with a homogeneous high-dose area inside the patient. These topics are discussed further in the proton therapy section below.

2.3.5 Range and multiple coulomb scattering

As the particle transverses through matter, it will continuously interact with the surrounding electrons and nuclei. Each collision varies in the amount of energy loss, and the final range of the particle is described as a statistical process and has a Gaussian likelihood distribution. The distribution is illustrated in figure 2.9 showing the mean range of transmitted particles as a function of absorber thickness. These individually different path lengths of each charged particle are often referred to as the range straggling, and it is a highly important factor to take account for in ion treatment [5].

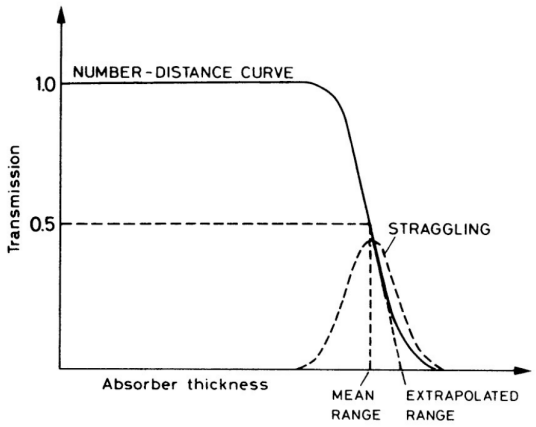

Figure 2.9: The ratio between incident and transmitted particles as a function of depth [7].

The range of a particle, for example, a Proton or a Helium nucleus, can be calculated numerically by integrating the Bethe equation, resulting in tables such as PSTAR/ASTAR [8], or it can be approximated from the initial energy E_0:

$$R = \alpha E_0^p, \tag{2.8}$$

where α and p are two parameters found by fitting experimental data. The often-used values are $\alpha = 0.002$ cm/MeV and $p = 1.77$ [5].

The particle will repeatedly undergo elastic interactions with the atomic nuclei as it transverses through a medium. These collisions have a negligible energy transfer but will add a small angle deviation from the particle's original trajectory. If the particle enters a medium with thickness x, it will be exposed to a large number of these collisions, which leads to an angular dispersion modeled as a Gaussian distribution [3]:

$$\theta_{plane}^{rms} = \frac{13.6MeV}{\beta pc} z \sqrt{\frac{x}{X_0}} \left[1 + 0.038 ln\left(\frac{x}{X_0}\right)\right], \tag{2.9}$$

where the angle θ is expressed in rad, the particle momentum p in MeV, and the velocity β in units of velocity of light c. The charge number of the projectile is z and x/X_0 is the thickness of the absorption medium in units of radiation length. Figure 2.10 shows the angular distribution on a measuring plane after a length L.

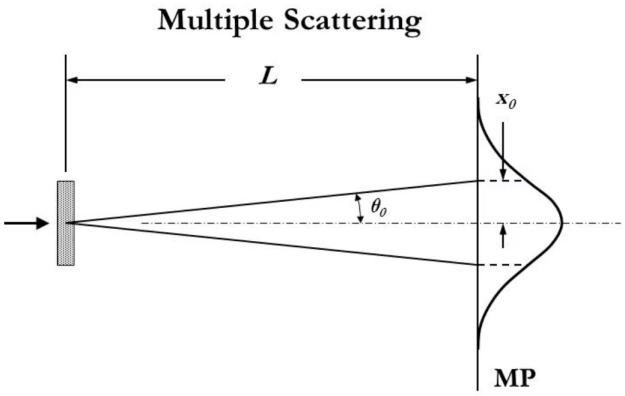

Figure 2.10: Angular dispersion in the measuring plane (MP) after a length L caused by Multiple Coulomb scattering in a thin slab [9].

This phenomenon is known as multiple scattering and is crucial for clinical ion radiation therapy in order to understand and estimate the particle's trajectory inside the patient. Also, the Multiple Coulomb scattering leads to challenges in proton imaging, as one has to track each proton in different layers in order to estimate the energy loss [5].

2.4 Radiobiology and dosimetry

As described in section 2.1, radiation can ionize and cause excitation of atoms in the absorbing material. If a living organism is exposed to radiation, it follows that these processes may break up molecular bonds. This can be extremely hazardous to the biological tissue as living cells may be killed and genetic material severely damaged [10]. In radiotherapy, one utilizes these effects to destroy cells that are harmful to the body, like cancer cells. The DNA molecules inside these cells consist of two chains (strands) wrapped around each other carrying genetic material and these are the primary target when treating with radiation. In order to kill a cell, one has to deposit enough energy so that a sufficient number of the DNA's double-strands break and the cell will then be unable to repair itself [11].

As stated before, the radiation can either be directly or indirectly ionizing. Both of these types of radiation may harm the biological tissue, in either breaking up the DNA strands directly or ionize water to produce highly reactive radicals which will then damage the DNA molecules.

In radiation dosimetry, the absorbed dose in a material is measured from the exposure of ionizing radiation. The dose quantity is often specified as gray (Gy) in mass or as sievert (Sv) in biological tissue, and both units are defined as the energy absorbed

per unit of mass J/kg. The absorbed dose can be used to describe the quantity of any ionization radiation absorbed in a material [1]:

$$D = \frac{\Delta E_{ab}}{\triangle m}, \tag{2.10}$$

where ΔE_{ab} is the absorbed energy and Δm is the mass of the medium.

Damage to biological tissue also depends on other factors, such as the ionization rate of the particle and the type of tissue irradiated. The quantity that describes the ionization density is known as the Linear Energy Transfer (LET). The LET is defined as the mean amount of energy that an ionizing particle imparts to an absorbing medium per unit length, expressed in keV/μm. It is closely connected to the stopping power of the particle but focuses on the energy deposition in the absorbed and not the energy loss of the particle itself. The LET is separated into low LET (sparsely ionizing) radiation and high LET (densely ionizing) radiation, and particles such as heavy ions, protons, and neutrons have a high LET while X-ray and γ-ray have low a LET. As high LET radiation is densely ionizing, it will damage the DNA more effectively, and has, therefore, more severe biological effects per unit of absorbed dose.

The effectiveness of different types of radiation can be assessed by comparing the ratio of doses needed to achieve the same biological effects. This number is called Relative Biological Effectiveness (RBE), and this quantity is closely related to the LET.

As the LET increases up to 100 keV/μm the RBE also increases up to a value of 4-5 compared to low LET radiation, meaning that the biological tissue is damaged more effectively. For higher LET, however, the RBE factor decreases as the dose produced by ionization exceeds the limit of individual cell death. Figure 2.11 illustrates the dose distribution for photons, carbons, and protons, showing the effects of the RBE factor. The protons and carbons deposit a small relative dose in the entrance of the medium as their LET, and hence RBE is small at high velocities. However, as the charged particles transverses the medium, their energy will gradually decrease. This will lead to an increase in the LET and hence, the Bragg Peak.

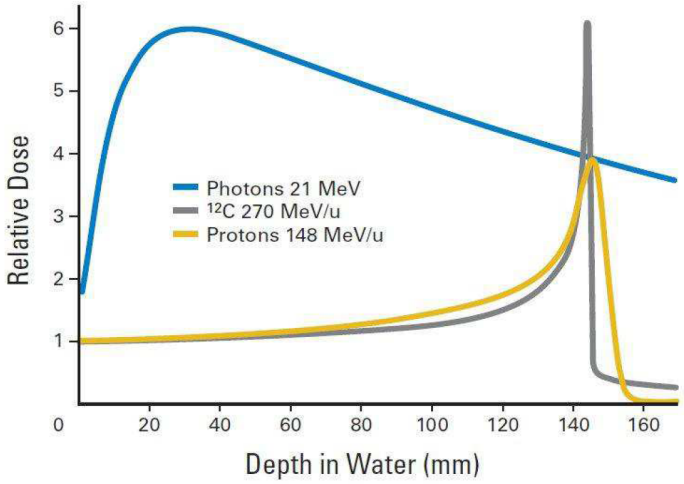

Figure 2.11: Relative dose distribution for photons, carbons and protons as a function of the depth in water [12].

Heavy ions might break up at the end and create nuclear fragments and will produce a tail in the Bragg peak, illustrated on the end of the gray curve. Their peak, however, is even sharper than for protons as carbon ions have a greater RBE. To have the ability to treat with different particles and ions is an advantage in clinical radiation therapy, as one has more freedom to tailor the radiation field to fit the treatment area best [1, 5].

2.5 Radiotherapy

The goal of radiotherapy is to use ionizing radiation to damage and destroy malignant tumors and at the same time minimize the dose to healthy normal tissue. Higher doses produce better control of the tumor, but must again be limited in order to prevent excessive side effects. The vast technological improvements in this field have created more freedom in how the tumor can be treated. Depending on the characteristics of the tumor, such as tumor type and location, one can modify the beam in a variety of means in order to treat the tumor the best way possible [13].

2.5.1 Photon therapy

In conventional external radiotherapy, one uses a linear accelerator to produce high energetic photons in order to damage and kill tumor cells. The photon beam attenuates as it transverses through the body and will deposit radiation energy along its path that damages the surrounding tissue. New photon technologies have made

considerable improvements in accuracy where one can treat the target more precisely, like shaping the beam field to increase the accuracy when irradiating the tumor. Today, the primary tool for this purpose is a multi-leaf collimator, a deceive consisting of many thin tungsten leaves which all can be moved individually. With this device, it is possible to shape the field in almost any desired shape automatically and efficiently, even during treatment sections [13].

In Intensity Modulated Radiation Therapy (IMRT), illustrated in figure 2.12, one uses advanced software to create radiation fields with varying shapes and intensity. The computer creates the final treatment plan after setting in dose constraints to the tumor and its surrounding tissue. This process is called inverse treatment planning since the specific dose has to be set first in order to make the treatment plan [14].

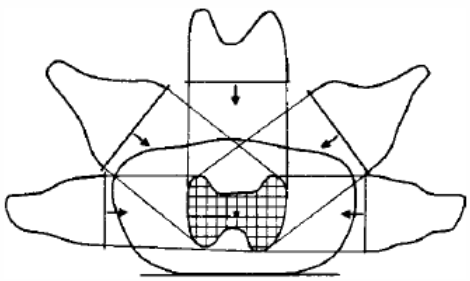

Figure 2.12: Illustration of the Intensity Modulated Radiation Therapy (IMRT) principle showing a number of intensity modulated beams together with their intensity profiles. Here, the hatched area is the target volume in an axial cut [14].

As we have discussed in section 2.2, the photon beam will gradually attenuate along its path, which means that the photon beam will deposit energy before and after the tumor target. No matter how good the technological aspects are, it is impossible to prevent this dose-effect completely. Both upstream and downstream damage will occur at the begging and exit of a photon beam. This issue with photons is the main reason for irradiating with ions, and this topic will be discussed in the next section [14].

2.5.2 Proton beam radiotherapy

In Proton Beam Radiation Therapy (PBRT) the Bragg peak is utilized to irradiate the tumor location accurately. The protons will deposit a large amount of its energy in a small area, and by setting the beam energy correctly, one can control the Bragg peak depth, and deposit the highest dose to the exact tumor location. This superior depth-dose characteristic of protons was pointed out in 1946 by Robert R. Wilson,

and the interest of PBRT has been increasing worldwide since because of its clear advantages over conventional photon therapy [5].

In order to accelerate the protons to high enough energy for treatment (200 to 250 MeV), a cyclotron can be used. This machine consists of a fixed magnet and two metal half-disks. The half-disks has a gap in between them, and they oscillate the electrical field such that the protons get accelerated every time they pass over the gap. The fixed magnetic is needed to bend the charged particle into a circular path so that it will cross the gap multiple times until the desired energy is achieved. One can also use light-ions in radiation therapy, like carbon ions. In order to achieve the same penetration length as for 150 MeV protons, one has to accelerate the carbon ion to 3000 MeV (250 MeV/μ). This amount of ion energy can only be delivered by a large, complex machine called a synchrotron [9].

The relative dose distribution for X-rays and protons are shown in figure 2.13. The Bragg peak area of the protons are determined by their energy, and this relation is utilized in proton therapy to create a spread out Bragg peak, indicated by the blue line in the figure. This method will accurately irradiate the tumor as the dose distribution is homogeneous in this area and falls quickly after the tumor location. X-rays, however, will deposit extra dose before and after the tumor location, leading to unnecessary irradiation to healthy tissue [9].

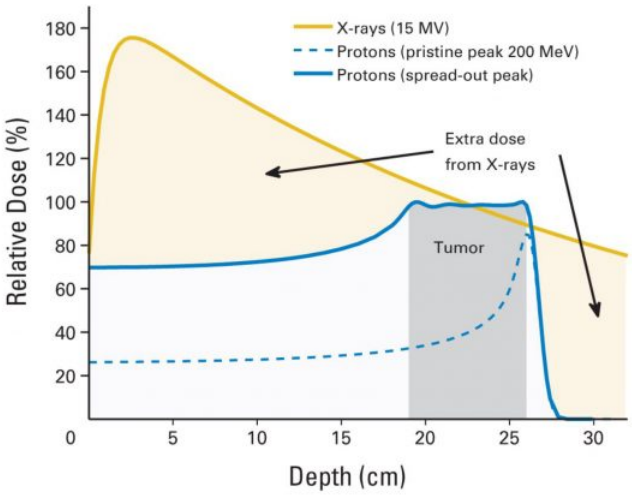

Figure 2.13: Dose deposited as a function of depth for X-ray (yellow line) and protons (dashed blue line). Notice that the protons have a spread out Bragg peak (blue line) that covers the tumor and then stops [15].

2.6 Medical imaging and proton CT

Medical imaging is the technique of using different image modalities to create an image of the interior of a body for both diagnostic and treatment purposes. Vast improvements in this field have been lead to more accurate treatment planning and are immensely helpful for creating the best treating plan. Many different image modalities are used in medical imaging. Ultrasound, for example, utilizes sound waves characteristics to produce images of the inside of the body. This technique is vastly used in clinical procedures such as to examine tissue, blood flow and to create real-time visualization of the processes of the interior of the body. Magnetic Resonance Imaging (MRI) provides spatial information based on the concentration of fat and water in different tissues without the use of ionizing radiation. Moreover, Positron Emission Tomography (PET) uses internal radiation processes (annihilation of the positron) to map the metabolic activity in cells and tissue [16].

In this section, we will only be discussing imaging with X-ray. This is because this technique is closely connected with proton CT in many aspects and its this modality which proton CT will aim to exceed.

2.6.1 Photon imaging

X-ray planar radiography and computed tomography (CT) utilizes the differential absorption coefficient of photons in tissue. As we have seen in section 2.2, this coefficient determines how effectively photons are attenuated when transversing through a medium. The absorption coefficient is dependent on the Z value of the material, and this means that a high Z value material, like bone, will absorb the X-rays more efficiently than soft tissue. One can then detect the photons with a detector mounted at the behind the patient and use the intensity detected to decide which material the photons have passed through. In the example figure 2.14, one can see a high contrast separation between the white high absorbent (bone) and dark light absorbent (lung tissue) [16].

Figure 2.14: Example of an image of the chest taken with planar radiography. The bones have attenuated the X-rays to a much higher degree than the soft tissue of the lungs and appear brighter on the image [16].

In a 3D CT scan, the X-ray beam and the detector rotates continuously around the patient and records a series of one-dimensional projections, as illustrated in figure 2.15. One can then use a process called filtered back projection to produce an axial slice of the body. One can obtain multiple slices by moving the patient table continuously in small steps in the head/foot direction. One will then acquire multiple adjacent 2D slices which can be put together to form a three-dimensional image of the interior of the body.

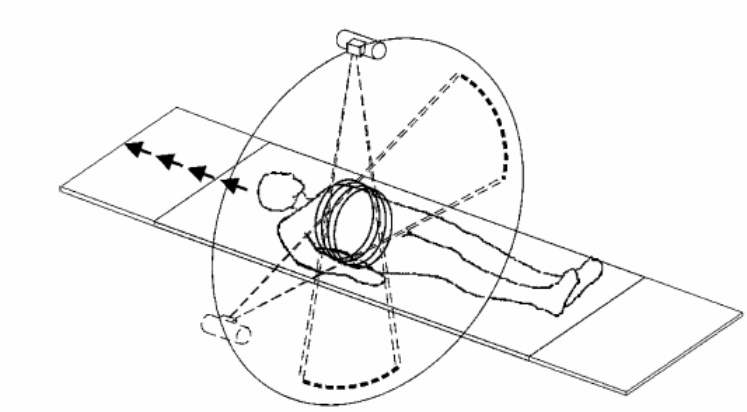

Figure 2.15: Illustration on obtaining a sequence of image slices in a fan-beam scanner for a 3D CT image [17].

Houndsfield Units (HU) (also called CT number) are used to define the degree of attenuation in various tissues. The Houndsfield number of a particular tissue is defined as [17] [16]:

$$HU_{tissue} = 1,000 \frac{\mu_{tissue} - \mu_{H_2o}}{\mu_{H_2o}}, \tag{2.11}$$

where μ_{tissue} and μ_{H_2o} are the X-ray attenuation coefficient for tissue and water, respectively.

For 70 keV photons, the Houndsfield units are -1000 for air and 1000-3000 for bone, where the highest number corresponds to dense bone. Each pixel/voxel in the image is assigned a HU number, so the CT image does not display the tissue attenuation coefficients directly, but rather a map of the tissue CT numbers.

2.6.2 Proton CT

In proton Computed Tomography (pCT), one aims to image the interior of the body by measuring the Stopping Power (SP) variations for different tissues by using proton beam energies above 200 MeV. The purpose of this imaging technique is to more accurately map the Relative Stopping Power (RSP) by measuring it directly with protons. The stopping power expresses the rate of energy loss of a charged particle per cm of the medium traversed. This quantity, as well as with accurate tumor location, is essential for proton therapy planning. Accurate RSP mapping is advantageous for a precise estimate of the proton beam range, which leads to more effective treatment and reduces the risk of healthy tissue irradiation [5].

Today, one uses 3D images obtained by X-ray CT first to find and map the Hounsfield Units (HU) of the tissues. These measurements must then be converted into stopping power by using a calibration curve. This converting method introduces range estimation uncertainties of the proton beam which, translated into the uncertainty of Bragg peak location. This “in between” converting step can be removed entirely with pCT as it measures the SP directly.

The goal for pCT is then to map the SP with an error below 1 mm. This task is complex and challenging, especially since Multiple Coulomb scattering leads to curved paths for protons and displacements of their incoming trajectory versus the outgoing one. Because of this effect, one has to individually track each proton before and after penetrating the object by using the position and angle information. This is illustrated in figure 2.16. One can then estimate the path that the proton took through the object, referred to as the Most Likely Path (MLP).

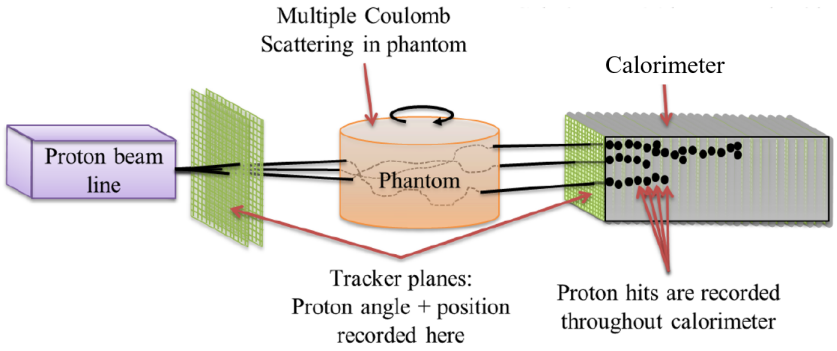

Figure 2.16: Setup of a proposed proton CT system [17].

In order to collect data fast enough for clinical proton imaging, high proton rates are needed. This challenges the detector in the demand of high resolution and fast readout speed needed for locating and separating the tracks. In order to map the SP, the energy of the protons has to be measured after traversing the imaging object. This is done by having a calorimeter in the back-end of the medium, as shown in figure 2.16. By simultaneously tracking and measure the energy of the protons, the individually MLP can be created, and each voxel inside the object can be assigned a stopping power unit [5].

2.6.3 Proton CT development at the University of Bergen

There is an ongoing project at the University of Bergen (UiB) which aims to develop a proton CT system for clinical use. This proton CT prototype is based on the use of a Digital Tracking Calorimeter (DTC) for both tracking and energy measurement of the protons. The DTC will consist of Monolithic Active Pixels Sensors (MAPS) for accurate and fast readout speed. As discussed in the previous subsection, the protons' position and angle have to be measured before and after the phantom, and the main idea is then to have a front and a back tracker. The latest updates on the Bergen proton CT system, however, consists of an idea to only use the backtracking calorimeter and a thin pencil beam to estimate the position and angle of the protons before and after the phantom. An illustrated of this setup is shown in figure 2.17. By excluding the front tracker, the complexities and the data rate of the system reduces, and this could be the right solution in getting a clinical working prototype with today's technology [5].

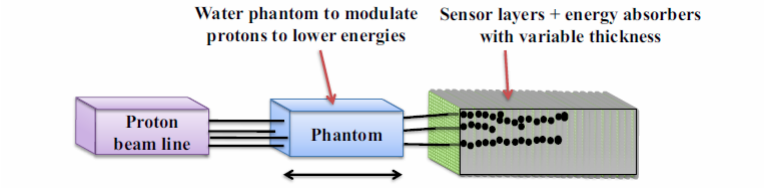

Figure 2.17: Setup for the proposed proton CT system at the University of Bergen. A thin pencil beam and a backtracking calorimeter will be used to measure the protons' path in the phantom as well as their energy loss [17].

CHAPTER 3

Silicon Pixel Detectors

This chapter summarizes the basics of semiconductors and how a charged particle is able to produce a signal in the material. The properties and design of silicon pixel sensors are discussed, and the chapter closes with a discussion of the advantages and disadvantages of Monolithic Active Pixels Sensors (MAPS) device. Finally, clusters on MAPS are discussed as well as the main parameters that influence the size of the clusters.

3.1 Silicon Semiconductor sensors

Semiconductor sensors became a common tracking device in particle physics in the late 1970s and are now become a crucial part in vertex tracking for high-energy physics experiments. The continuous development of such detectors has primarily been triggered by the requirements of having a high granularity device with a good space and time resolution. Such detector properties are also appealing for medical imaging devices, especially in X-ray CT imaging to detect and separate optical photons, and in proton CT for tracking purposes [3].

These semiconductors are solid-state detectors based on the principal of energy loss of traversing particles or radiation. When a particle transverses through the sensor material (which is in almost all cases silicon) an amount of the energy will be deposited, which will ionize the medium and create electron-hole (e-h) pairs. This deposited energy, generated as e-h pairs (often referred to as charge carriers), can be detected as an electrical signal due to their motion.

3.1.1 Charge generation in silicon semiconductors

The number of electron-hole pairs generated is dependent on the sensor material and the amount of energy deposited. In silicon, the mean energy needed for creating an

electron-hole pair w is about 3.6 eV. So the average number of electron-hole pairs N generated by an amount of absorbed energy E is [3]:

$$N = \frac{E}{w}. \tag{3.1}$$

An amount of the energy deposited can also go to producing thermal energy, causing the number of generated e-h pairs to fluctuate. Therefore, the factor F (Fano Factor) can be applied in order to calculate the mean-variance:

$$\left\langle \Delta N^2 \right\rangle = FN = \frac{FE}{w}. \tag{3.2}$$

This Fano factor is around 0.1 for most semiconductors [3].

3.1.2 P-N junction and the depletion zone

The PN-junction is a fundamental building block of silicon semiconductor sensors. It is created by doping two semiconductors giving them a higher concentration of either electrons (n-doped) or holes (p-doped). When putting these two materials together, allowing a transition between the n-doped and p-doped material, the electrons and holes will diffuse to either side and recombine. This zone, formed by the PN-junction, is called a depletion zone (space charge region) as it is depleted from free charge carriers. The space charge region creates a potential difference, and this electrical field counteracts further diffusion of the electrons and holes [3].

A particle traversing into the depletion region, will then ionize the medium and create electron-hole pairs. These charge carriers will be exposed to the electrical field, created by the space charge region, and drift towards the collecting electrodes and generate a signal.

3.1.3 Transportation of charge carriers

The charge carriers generated by the ionizing particle has to move to the electrical contacts in order to produce the electrical signal which is picked up by the readout electronics. Free charge carriers move randomly and can is considered as free particles with mean kinetic energy depending on the temperature T of the silicon semiconductor [3]:

$$KE_{avg} = \frac{3}{2}kT, \tag{3.3}$$

where k is the Boltzmann's constant. Their mean thermal velocity is around 10^5 m/s with a mean free path in the order of 0.1 μm. The charge carriers will continuously collide and the mean time τ_c between each collision is about 10^{-12} seconds.

3.1.4 Diffusion

The charged particle interacting with the silicon will liberate a large number of electron-hole pairs. In the center of this production, there will be a high consecration of charge carriers. These charge carriers in the high concentration region will spread toward low concentration regions. This is due to the random movement of charge carriers, which implies that a high concentration of charge carriers is more probable to spread to low concentration regions than vise versa. This spreading effect is called diffusion and can be described as a Gaussian distribution away from its center with a standard deviation [3]:

$$\sigma = \sqrt{2Dt}, \tag{3.4}$$

after a time t and where D is the diffusion constant. This Gaussian distribution at different times t is plotted in figure 3.1.

Since electrons diffuse faster than holes, the diffusion constant can be written as $D_{n,p}$ to describe either electrons (n) or holes (p). This constant is related to the mobility of the charge carriers via the Einstein equation $D_{n,p}/\mu_{n,p} = kT/e$. Here, e is the electron charge, T is the temperature and $\mu_{n,p}$ is the mobility for either the electron or proton.

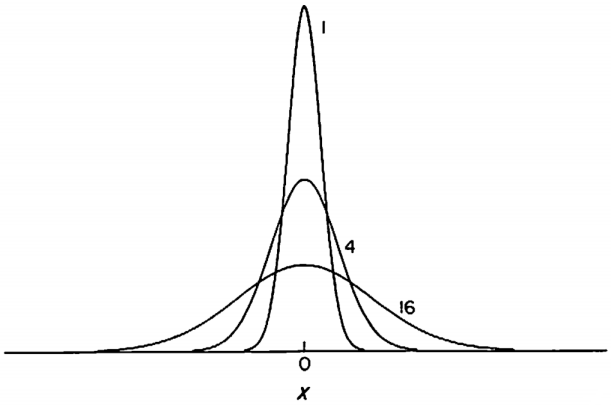

Figure 3.1: The probability of finding particles at different points x at times $t = 1$, 4 and 16. This is a Gaussian distribution centered at the $x = 0$ position where the particles originated from [18].

The diffusion current per unit area is described by [3]:

$$J_{n,diff} = -D_n \nabla n = -\frac{kT}{e}\mu_n \nabla n, \tag{3.5}$$

$$J_{p,diff} = D_p \nabla p = -\frac{kT}{e}\mu_p \nabla p, \tag{3.6}$$

for electrons and holes respectively. Where ∇n and ∇p are the gradients of the electrons and hole concentration. The diffusion current can be derived from equation 3.4 by approximating the charge carrier concentration at a position x away from the center. This method is illustrated in figure 3.2.

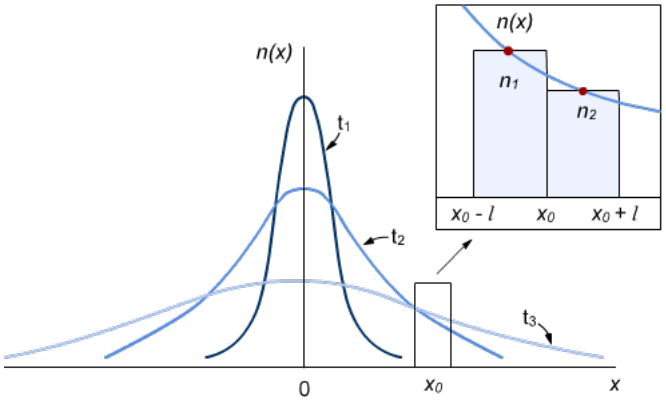

Figure 3.2: By approximating the charge carrier concentration n at a position x, one can derive the diffusion current per unit area (equation 3.5 and 3.6) [19].

3.1.5 Drift

When an external electrical field is applied, the charge carriers will accelerate between random collisions. Even though the electrical field accelerates the charge carriers, their overall velocity will still not increase with time since they are continuously slowed down by the collisions. This average drift velocity is in the direction of the electrical field and is given by [3]:

$$v_n = -\frac{e\tau_c}{m_n}E = -\mu_n E, \tag{3.7}$$

$$v_p = -\frac{e\tau_c}{m_p}E = \mu_p E, \tag{3.8}$$

for electrons and holes respectively. In these two equations, v is the average drift velocity, m the effective mass of electrons (holes), and E the electric field.

For high electrical fields, the acceleration and collision will counterbalance each other out in such a way that if the acceleration increases, the collision rate will also increase. The mean free path of the charge carriers is not altered by the field, leading to a saturation in the drift velocity, shown in figure 3.3.

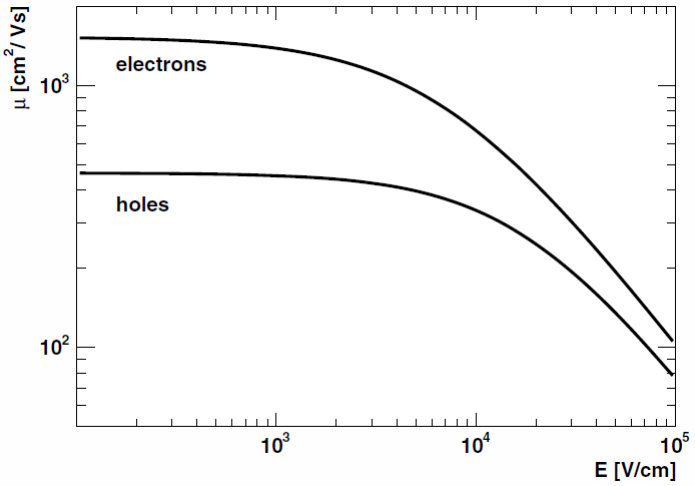

Figure 3.3: The mobility for electrons and holes as a function of the strength of the electrical field [3].

In intrinsic silicon where the electron field is low, the mobility at 300 K is given as [3]:

$$\mu_n = 1,415 \pm 45 \ cm^2/(\text{Vs}),$$

$$\mu_p = 480 \pm 17 \ cm^2/(\text{Vs}).$$

As seen from these numbers, the electrons move around three times faster than the holes.

3.2 Pixels

In image processing, the notion of "pixel" (short for picture element) is used to describe the smallest controllable element in a device. A pixel detector is a device consisting of these pixels and is able to capture an image. A large pixel area means that one can detect an image of a larger size, and the pixel pitch/size of the pixels will then correspond to the granularity of the image (described in section 1.4). Each pixel has a sensitive area in which an ionizing particle will create a signal which can be detected and is read out by the electronics [3].

A typical example of a pixel detector is the digital camera, which generates an image based on the intensity distribution of the detected photons. The sensing elements in

each pixel detect the photons during a short exposure time and can then map the intensity difference to create an image[1].

There are a variety of different pixel detectors with diversity in the underlying techniques used in the process. The pixels detectors used in high-energy physics needs to be fast (i.e., able to take millions of pictures per second) and sensitive to high-energy particles and electromagnetic radiation. Such pixel detectors also have properties that are beneficial for pCT, in which one needs to detect and track multiple high-energy protons in a short amount of time. The following section will discuss this specific theology in more detail.

3.2.1 Monolithic Active Pixel Sensors (MAPS)

A pixel is said to be "Monolithic" if the sensor, amplification and the readout circuit are all integrated into the pixel itself. This idea of a monolithic device is appealing in many applications since these pixels offers low noise figures and reduced production costs, compared to hybrid pixels where the sensor and amplifying/readout chip are separated [20, 3].

The sophisticated electronic design of Monolithic Active Pixel Sensors (MAPS) is achievable by integrating the electric parts on a thin layer of p-doped silicon. This is done by using CMOS (Complementary Metal–Oxide–Semiconductor) technology and today; the CMOS circuit can be manufactured on a high resistivity epitaxial layer which gives high voltage diodes.

When a signal charge is generated in the p-type epitaxial layer, it can reach an n-well collection diode by thermal diffusion. Then the charge is collected by drift present in the depletion region and then pushed to the electrodes via an additional electrical field. This diffusion process leads to a reduced charge collection time and hence increasing the probability of the signal charge to be lost before readout. The MAPS structure (figure 3.4) shows that the depletion region only occurs directly under the n-well collection diode. Here, a full charge collection is obtained unlike most of the epitaxial layer where it is incomplete.

[1] If one also applies a color filtering for each of the three primary colors, one can combine these intensities to create a color image.

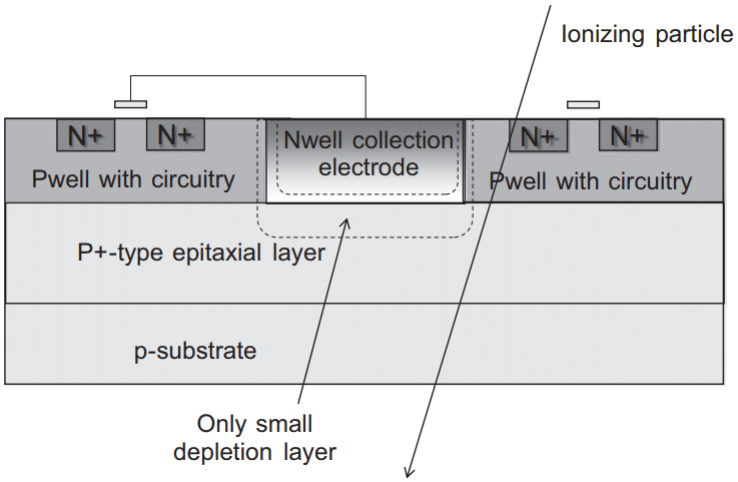

Figure 3.4: Cross section of a MAPS detector showing the small depletion region under the n-well [20].

3.3 Clusters on MAPS

A pixel is said to be fired when the charge collection exceeds the charge threshold set by the readout electronics. If the charge deposited from a single particle is sufficiently high, this charge can be shared between adjacent pixels. This group of firing pixels, showing a shared signal from the same particle, is called a cluster.

For a binary readout electronic (hit/not hit), the position resolution can be determined from the pitch p. The pitch is the distance from the center of one pixel to the next adjacent pixel. If only one pixel is fired, then the arrange difference between the true impact position x and the measured impact position x_m is given by [3]:

$$\sigma_{position} = \frac{p}{\sqrt{12}}. \tag{3.9}$$

In the case of a cluster, where more than one pixel is fired, the position resolution increases. For a charge sharing region with length s, the position resolution is then $s/\sqrt{12}$, and the $(p-s)/\sqrt{12}$, when only one pixel is fired. The difference in the position resolution with and without charge sharing is illustrated in figure 3.5.

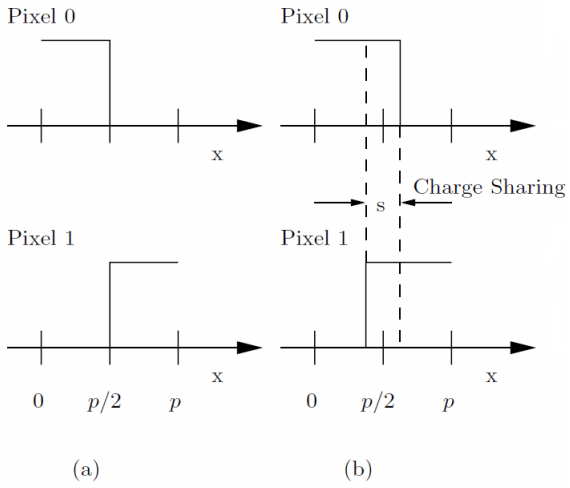

Figure 3.5: Signal (Y-axis) on two adjacent pixels as a function of the impact position x of the particle. A detector without charge sharing is shown in (a), and with charge sharing is shown in (b), both having a binary readout [3].

3.3.1 Clusters size

The charge collection method mentioned for the CMOS MAPS structures driven by thermal diffusion. The charge has then the capability of spreading to adjacent pixels and create clusters. For a large cluster, the charge divides over many pixels and reduces the effective signal-to-noise ratio. The information is also more significant for a wider cluster, and this requires more memory space, or dedicated processing circuitry to reduce the data before storage [20].

The size of these clusters on MAPS can change depending on [21]:

i) Momentum and particle type

ii) Operating environment

iii) Threshold and back bias settings

As discussed in the previous chapter, the energy deposition by a traversing particle is dependent on the particle type and its momentum. For a large energy deposition, the number of electron-hole pairs will be higher compared to a low energy deposition. As described in section 3.1.4, a higher density of charge carriers leads to a faster rate of diffusion. This means that the charge carriers can spread longer distances the higher the concentration of charger careers are at the initial state. In the end, this will lead to more pixels firing as the charge carrier reaches further adjacent pixels.

The diffusion rate is also dependent on the temperature of the medium, as shown in equation 3.4 to 3.6. In a higher temperature environment, the charge carriers

will diffuse faster, and this will again influence the size of the clusters as the charge carriers can reach further pixels.

The threshold setting of the MAPS detector decides how much charge that is needed to fire a pixel. With a lower threshold setting, less charge collection is required in order to fire a pixel. The charge sharing between adjacent pixels are, therefore, more likely to become sufficient to fire those pixels, and thus creating larger clusters. Figure 5.22 shows the fraction of clusters vs. their pixel size at different I_{thr} values for a MAPS chip irradiated with Minimum Ionization Particles (MIPS).

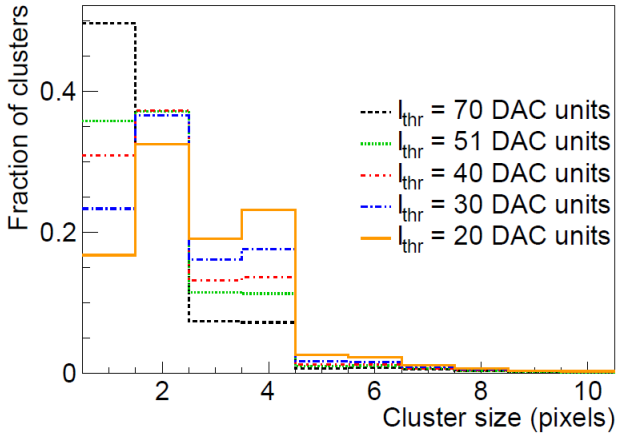

Figure 3.6: The cluster size distribution at V_{bb}= 0 V for different I_{thr} values. A Digital-to-Analog Converter (DAC) unit is a value representing the charge threshold for the chip. The figure shows that for a lower threshold value, the fraction of larger clusters increases [21].

The last point mentioned is the back bias voltage setting on the MAPS detector, and by applying a reverse substrate bias, the depletion region will change significantly. An increase of the bias will deplete a larger part of the epitaxial layer, and hence, the electrons can reach a depletion region easier by diffusion. This also means that fewer pixels are fired since a large depletion region limits the diffusion capability to adjacent pixels. This is shown in figure 3.7 for MIPS [20, 21].

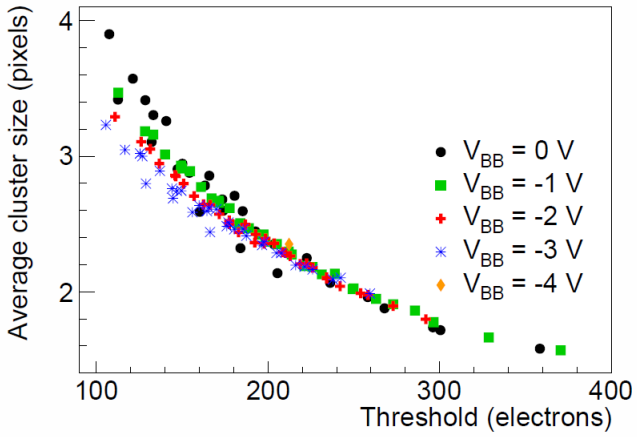

Figure 3.7: The average cluster size distribution for different V_{bb} and threshold for a MAPS chip. The plot shows that the cluster size decreases for a higher applied reverse-substrate-bias value, and that this change is more noticeable at lower threshold values [21].

CHAPTER 4

The ALPIDE chip

This chapter aims to describe the basics of the ALPIDE chip focusing on its readout electronics. The chips trigger and strobe signals are discussed to explain how firing pixels are latched into the memory. In the end, the function of the ALPIDE in the DTC is presented, highlighting the use of the clusters produced in the chip for both tracking purposes and range estimations.

4.1 The ALPIDE chip

The ALPIDE chip is a CMOS Monolithic Active pixel sensor developed at CERN with the aim of improving the read-out rate as well as position and momentum resolution of ALICE (A Large Ion Collider Experiment). ALICE is one of the seven detectors at CERN which are stationed around the LHC (Large Hadron Collider). The ALICE experiment will have a shutdown from 2019 to 2020 where the inner tracking system (ITS) of the detector will be upgraded. A new ITS design is based on installing seven large silicon tracker layers, three in the inner barrel (IB) and four the outer barrel (IB). It is the ALPIDE chip that will be used in these layers [22]. A picture of the ALPIDE chip is shown in figure 4.1.

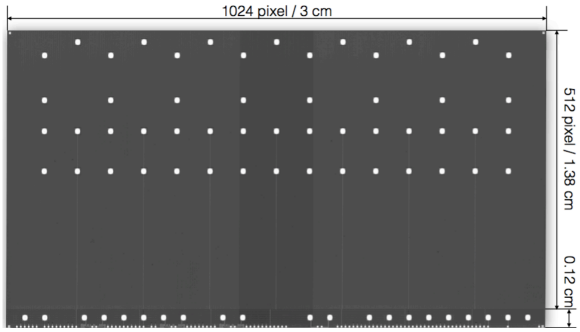

Figure 4.1: A drawing of the ALPIDE chip showing its size. The white spaces on the chip are interface pads used for wire bonding [23].

The ALPIDE chip is 15 mm × 30 mm in size and contains a matrix of 512×1028 pixels with a binary readout (hit/no hit). Each pixel is 28×28 μm^2 with in-pixel amplification, shaping, discrimination and a multi-event buffering. This technology is provided by Towerjazzz's 180nm CMOS imaging process. The electronic circuits are fabricated on a high-resistivity epitaxial silicon layer. A particle crossing the epitaxial layer produces electron-hole. The electrons can then diffuse laterally towards the sensing diode as they are being confined vertically by the potential barriers. This is illustrated in figure 4.2. These potential barriers are created by the p-wells and the p-type substrate. The sensing diode is a n-well with $\sim$ 2 μm in diameter, about 100 times smaller area than the pixel area itself [23].

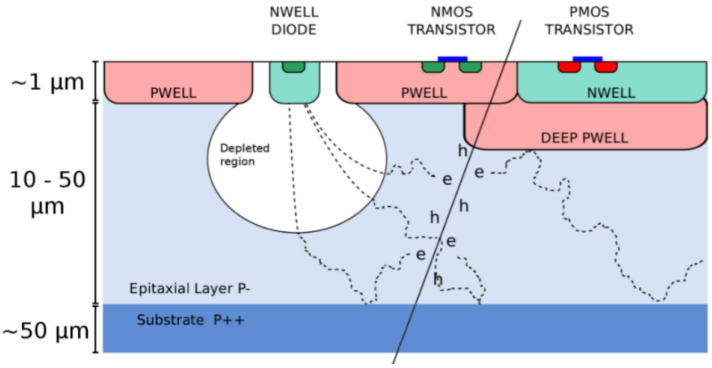

Figure 4.2: Illustration of a cross section of the ALPIDE, showing the charge collection mechanism [23].

When the electrons reach the depletion zone of the diode, they will induce a current signal. The charge carriers can also be produced directly inside the depletion zone if the charged particle transverses this part. This depletion volume around the n-well can also be increased by applying a reverse bias voltage, leading to a higher S/N

ratio. This signal is then amplified and shaped, as illustrated in figure 4.3, and must exceed a fixed threshold value in order to be sent forward by the discriminator. The peaking time of the front-end is in the order of 2 μs while the discriminated pulse has a duration of around 5-10 μs. The front-end acts as a delay and enables the ALPIDE to be run in trigger mode, as the delay of the front-end is larger than the trigger latency. The trigger produces a strobe signal, and if the strobe signal is present at the same time as the front-end output charge pulse, the signal gets stored. These digital signals are stored in the three in-pixel memory cells which can be read out by the priority encoders. The priority encoder will reset the pixel afterwards, and the cycle can continue [22, 23].

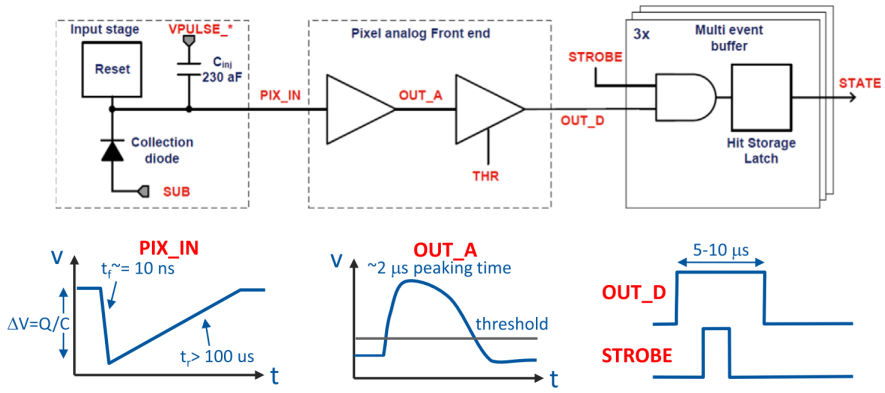

Figure 4.3: Block diagram of the circuit stages in the ALPIDE pixel. The induced current signal is amplified, shaped before it reaches the discriminator. Only signals that exceeds the threshold and matches up with the strobe will be stored [23].

4.1.1 Triggering and strobes

The ALPIDE can be run in either trigger mode or continues mode. In trigger mode, the strobe signal typically comes from an external detector source, such as the first level trigger in ALICE or, for example, a fast plastic scintillator. The ALPIDE would then only receive a trigger when there is a particle detected in the external source. Each trigger produces a strobe, and the user can set the strobe duration. With the correct settings, the strobe signal produced in this trigger mode should always match a front-end signal. Hence, if the strobe duration is long enough to capture the whole charge signal, there should be no empty frames captured by the trigger and the whole charge signal would be captured in a single frame [21]. This is illustrated in the bottom right diagram in figure 4.3.

In continues mode, however, the ALPIDE receives periodically repeated triggers, for example by a signal pulse generator. This trigger frequency is then set by the user.

The output of the DAQ board is limited by the connection to the host computer, and in many cases, a readout pause has to be introduced somewhere after a sequence of triggers. Such a sequence is referred to as a trigger-train, and after each trigger-train follows the readout deadtime of the detector. To be able to separate the events in a trigger-train, the strobe duration has to be less then the trigger period, if else, the strobe will be present indefinitely during the trigger-train, and it would be impossible to separate the events. However, if the strobe is much smaller then the front-end signal, this will introduce additional deadtime in the detector. So what is usually done, is to have a strobe signal just smaller than the trigger period, in order to decrease dead time and to be able to separate the events [21].

In continues mode, the triggering signal also comes randomly to the front-end signal. This means that front end- signal from one pixel can be latched into two different strobes. This creates two consecutive frames which both has the signal dived between each other, as illustrated in figure 4.4.

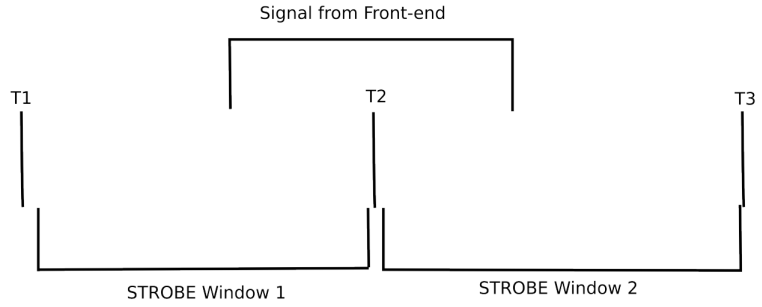

Figure 4.4: Illustration of the signal from the front-end discriminator being stored in two frames from the first trigger (T1) and the second trigger (T2) [21].

If one introduces more pixels, which get fired at different times due to the diffusion process, this can create a scenario as shown in figure 4.5. Then some of the pixels are only visible on the first frame, while the others are visible in the next frame.

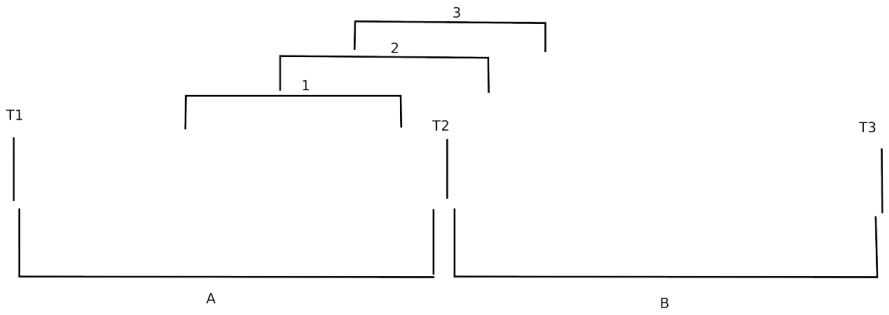

Figure 4.5: Signals from the front-end produced by the pixels 1-3. In this scenario, the pixels gets fired at different times due to diffusion and their signal is, therefore, registered at two consecutive frames [21].

4.2 The ALPIDE chip in the DTC

As stated in chapter one, the ALPIDE chip will be used in the pCT prototype. Nine of these chips will be mounted horizontally to a single carrier board, and several of such carrier boards will then be stacked vertically. The main purpose of the DTC is to determine the energy loss of each individual proton. When a particle transverses into the DTC, it will cross the ALPIDE layers and liberate charge carriers, producing clusters. By calculating the Center of Gravity (CoG) point from each cluster, one can reconstruct the path of the proton. Figure 4.6 shows such a reconstructing track algorithm, where tracking is done by choosing the CoG points (indicated by the yellow and green star) which has the smallest angle in between each layer [5].

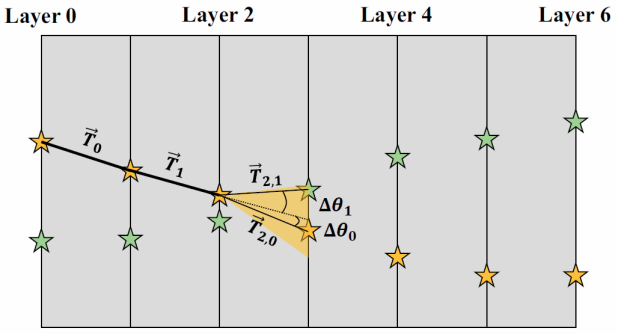

Figure 4.6: Schematic illustration of a track reconstruction process, with clusters from two protons. The continuation of the track $\overrightarrow{T_1}$ is chosen to be the smallest angle $\triangle\theta_0$ to the next track segment [5].

After the track reconstruction, one can calculate the energy loss of the proton by estimating the range traveled inside the DTC. This is done by looking at the number of layers that the particle has been able to penetrate. The range accuracy for this method is determined by the number of layers one has in the DTC and how far apart they are separated [1]. When the range has been estimated, one can, for example, use the Bragg-Kleeman formula (described in section 2.3.5) to calculate the initial energy E_0 which is again equal to the energy deposited by the particle inside the DTC.

There is also a common method used to supplement these range calculations and improve its accuracy. As we have seen, each track is reconstructed from a collection of clusters; hence there is only one cluster in each layer for each reconstructed track. One can use these cluster sizes to estimate the energy deposited in each layer by the proton. As discussed in chapter three, a larger charge deposition will lead to a larger cluster. This can be modeled with the function [5]:

$$n = aE_{dep}^{b}, \tag{4.1}$$

where n is the number of pixels in a cluster (cluster size), E_{dep} the energy deposition of the particle and a, b are two fitting parameters. One can then fit the Bragg peak using the Bragg-Kleeman rule to each of these energy deposition points along the track, as shown in figure 4.7.

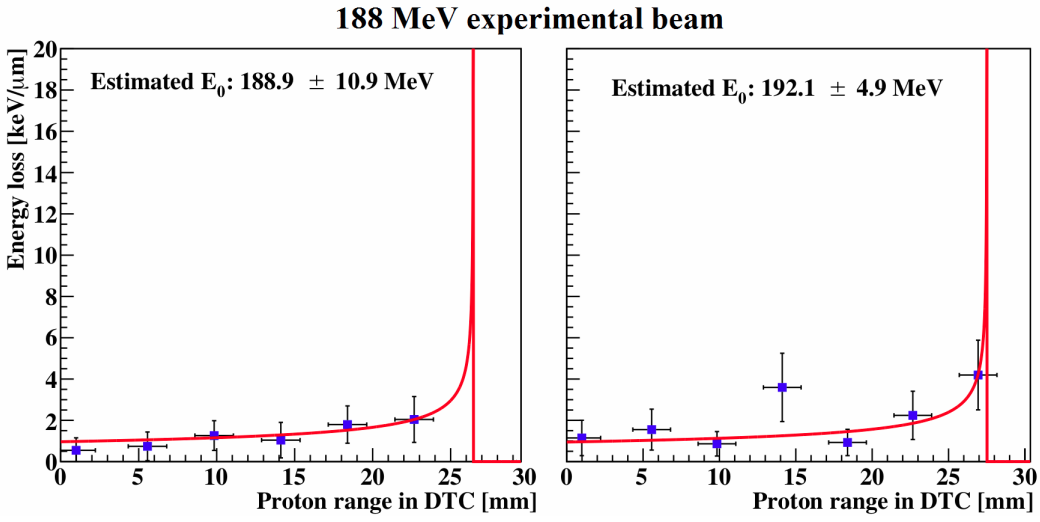

Figure 4.7: A Bragg curve fit along two individual proton tracks. The blue data points indicates the energy deposition in each layer, estimated from the cluster sizes [5].

[1] With a larger DTC one can measure a higher spectrum of energies, but a smaller distance between each layer will increase the accuracy of the estimated range.

This method was implemented and tested by Helge Pettersen in his P.hD. project in 2018 on the pCT DTC [5], and it leads to an increase in the absolute accuracy of the range estimation by 10% and the relative accuracy (not including the range straggling) by 50%.

CHAPTER 5

Characterization of the ALPIDE

This chapter begins with a brief analysis of a cluster development taken with an alpha source in the laboratory at the University of Bergen. Then, the analysis of the data taken with a helium microbeam at the Australia Nuclear Science and Technology Organization (ANSTO) is presented. Ph.D. student Andreas Tefre Samnøy conducted the experiment in January 2018. The equipment and setup are outlined here, together with a description of how the chip was scanned by the beam. It follows by a study of the threshold and noise values on the chip, focusing on the radiation-induced effects on the scanned regions. An experiment on cluster size vs. temperature conducted at the University of Bergen is presented in the end.

5.1 Experiment on cluster development

The purpose of the experiment was to investigate how clusters created by high energy depositions in the ALPIDE's epitaxial layer develops with time. This was achieved by irradiating the chip with an ^{241}Am source, producing alphas with an energy of around 5.5 MeV. The source had a particle rate of 3 kHz, and by setting the trigger frequency high enough, the same cluster was captured multiple times in consecutive frames. The experiment was conducted at the University of Bergen together with M.Sc. Viljar Eikland [21].

5.1.1 Experimental setup in Bergen

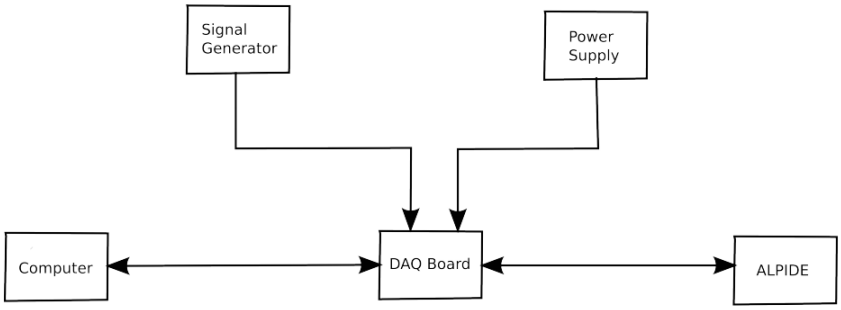

Figure 5.1: The experimental setup in the laboratory at the University of Bergen [21].

Figure 5.1 illustrates the setup of the experiment. The ALPIDE chip was connected to the Data Acquisition (DAQ) board, and the DAQ board was connected to a computer via a micro USB cable. The computer handled the communication and storing of the data from the ALPIDE chip. The DAQ board needs 5 V to run, and this was provided by a power supply. The power supply can also provide a reverse bias voltage to the chip, but during this experiment, the reverse back-bias voltage was kept at 0 V. This setting of the back-bias voltage was chosen to create the largest clusters in order to study its development clearer.

The ALPIDE received triggers from a signal generator which sent 3.3 V amplitude signals with a 150 ns width via the DAQ board into the chip. The generator sent 1000 of these triggers with a frequency of 1 MHz (1 μs period). Because of the limited throughput of the DAQ data output (USB3 bitrate), this sequence was followed by 100 ms silence in order to let the DAQ board handle and send the data to the host computer. At this configuration, the ALPIDE only collected data for 1 ms, which corresponds to around 1% of the whole 101 ms period.

The high frequency rate of the trigger was set in order to capture the same cluster several times during the charge sharing process. The strobe duration of the chip was set to 750 ns, and I_{thr} the was set to its default value at 50 DAC units. One DAC unit corresponds to around 7 e^- [24].

5.1.2 Results

The plots in figure 5.2 show a cluster created by an alpha particle captured in consecutive time frames. Each frame has an event ID number corresponding to the

time of the event, and with a strobe of 750 ns, there is a 250 ns deadtime between each of these frames. As discussed in subsection 4.1.1, depending on the deadtime between each trigger, a charge signal may still be present after the strobe from the first trigger. If the signal has been latched into memory by the first strobe and read out, the memory will reset, and the same signal can be latched into the memory again. This is exactly what happens in figure 5.2 as the trigger rate was high enough to cause the pixels to get latched into memory several times, and the same cluster then appears in multiple consecutive frames.

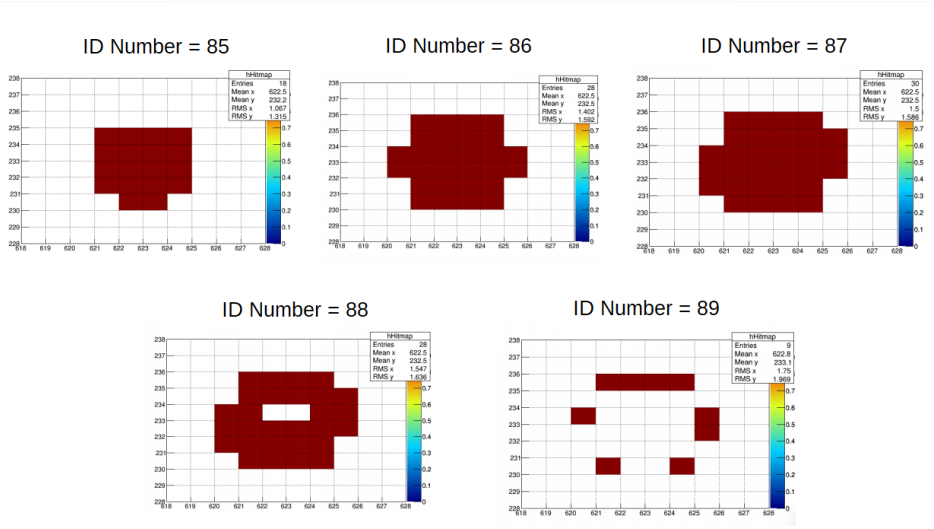

Figure 5.2: Hitmaps showing the evolution of a cluster for an alpha particle, captured in five consecutive frames (ID number from 85 to 89)

However, the plots in figure 5.2 also show, as time increases, the cluster evolves and change. In the first three frames, its size increases with time. This phenomenon comes from the diffusion of the charge carriers. As discussed in subsection 3.1.4, the distribution of a high concentration region of charge carriers has as a Gaussian shape, and due to diffusion, the distribution broadens with time. Hence, the pixels closest to the deposited charge will receive charge carriers first and be fired earlier than the pixels further away.

In the last two frames, after the diffusion process has finished firing newer pixels, the middle of the cluster starts to disappear. These pixels in the middle of the cluster has received a large charge and are discharged electronically, resulting in end-frames where the center of the cluster has vanished. In addition to this, it also takes longer time for the charge to reach pixels further away from the center. Therefore, the pixels in the periphery of the cluster will collect the charge at a later time compared to the middle pixels. This can also influence the chance of observing firing pixels in the boundary of the cluster after the center pulse charge has vanished.

This study of the cluster development was essential in understanding the cluster shapes obtained at the ANSTO experiment, presented in the next section.

5.2 Experiment on cluster size vs. beam position

The purpose of the experiment was to see if the cluster size would stay the same or vary with the position of where the energy was deposited. This was carried out by scanning the chip with a high-resolution mono-energetic beam with small steps between each beam spot, as illustrated in figure 5.3. The helium microbeam was provided by the ANSTO facility [12].

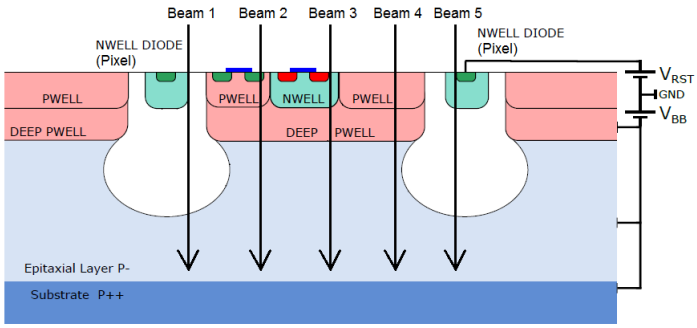

Figure 5.3: Illustration of how the ALPIDE chip was scanned.

5.2.1 Beam specifications

A Helium-4 ion beam was used with an energy of 10 MeV. In this energy range, helium deposits sufficient energy to create large clusters in the chip, which would make it easier to look for cluster size variations. The 10 MeV energy was also chosen so that the energy deposition would vary less since this energy range is outside the Bragg Peak. The microbeam at the ANSTO facility has an excellent resolution with a beam spot of less than 1 μm in diameter and can be moved in steps of 1 μm. The high-resolution beam was necessary in order to observe the cluster size variations inside the pixels.

The beam frequency was set on either 2 or 10 kHz, depending on which scan that was conducted. At this frequency, the rate of pileup events should be very low since the trigger rate is sufficiently higher (100 kHz). The dwell time, which is the beam time duration for each position, was in-between 100 ms to 300 ms also depending on the scan. Later, however, it was discovered that either the dwell time and the beam frequency should have been higher due to the readout deadtime which caused some beam spots to register no hits.

5.2.2 The ALPIDE setup

The ALPIDE chip was mounted inside a vacuum chamber, and it was slightly tilted by about 5 degrees due to space limitations inside the chamber. The beam was, therefore, not competently perpendicular, which would have been the ideal scenario. However, because of the vacuum chamber, the beam was not deteriorated by air or any beam exit before it hit the detector. Pictures of the ALPIDE setup inside the vacuum chamber are shown in figure 5.4 and 5.5.

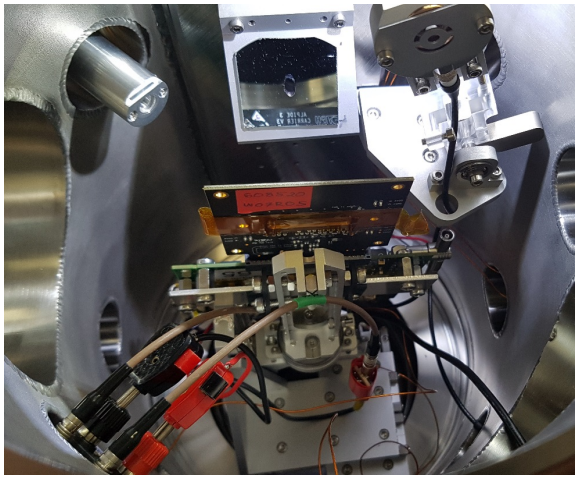

Figure 5.4: A top view of the setup showing the ALPIDE chip inside the vacuum chamber facing the beam exit.

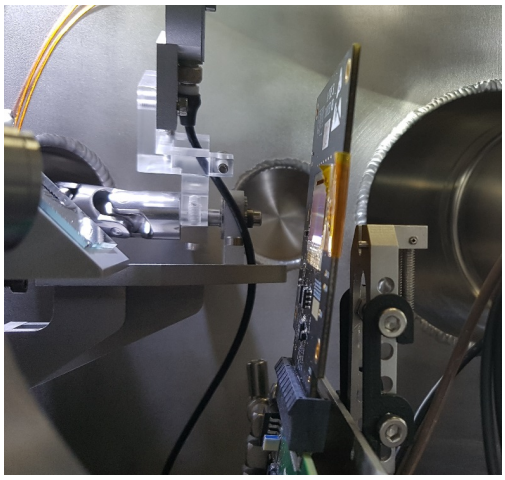

Figure 5.5: A side view of the setup showing the small tilt of the chip inside the chamber.

A few pixels were irradiated by the helium beam in each scan, and these runs were done twice with the same beam parameters. In the first scan, the back bias voltage of the ALPIDE was set to 0 V, and in the following scan it was changed to -3 V. The ALPIDE chip can also be used with a V_{bb} = -6 V, but this setting yielded many noise pixels and was therefore not applied.

The signal generator sent 100 triggers with a frequency of 100 kHz (10 μs period), and the strobe duration was set to 9.75 μs. The rest of the settings were the same as for the Bergen experiment.

5.2.3 Scanning of the chip

The chip was raster scanned using two distinct patterns at different areas on the chip. The most used pattern was a square, where the beam scanned 128×128 spots, starting from the bottom left and ended at the upper right corner of the area. This

pattern is illustrated in figure 5.6. If the beam finished scanning the 128×128 spots, its pattern reversed, and this could have led to that some of the last beam spots were scanned twice.

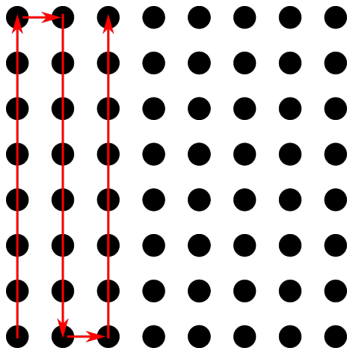

Figure 5.6: Schematic illustration of the square beam scanning pattern.

5.3 Raw data plots

The highest resolution beam patterns were obtained by having the spot pitch equal to 1 μm. These runs gave a more detailed picture of how the size of the clusters varied inside the pixels. Therefore, the following results focus on the 1 μm pitch data sets. In these data sets, the dwell time varied between 100 ms and 200 ms. The 200 ms runs is then favored because those runs have higher statistics for each beam spot position.

5.3.1 Raw hit maps

The following figures show raw hit maps of the of the square 128×128 μm^2 scans with V_{bb} = 0 V and V_{bb} = -3 V. It is important to notice that this area corresponds to around 4.5 pixels (128 μm / 28 μm) in the x and y-direction (roughly 20 pixels in total). These hit maps were obtained by simple plotting the x and y coordinate of the firing pixels.

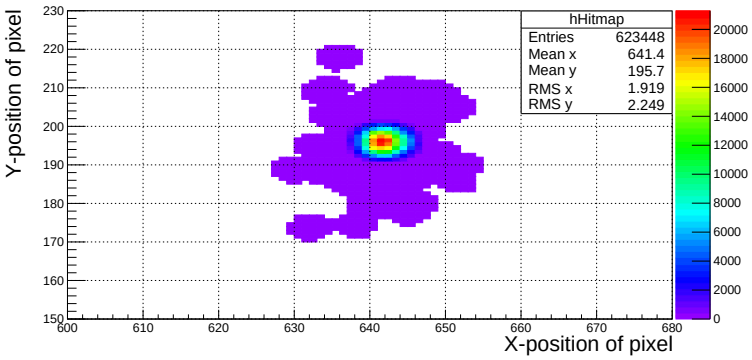

Figure 5.7: Raw hitmap of a 128×128 μm^2 scan with $V_{bb} = 0$ V.

Figure 5.7 shows, as expected that there is a high occupancy of firing pixels in the center of the scan. The purple area is pixels outside the scanned region which are only fired once and hence, must have been hit individually by single particles. As the beam has micrometer precision, it is highly unlikely that these areas originated from position uncertainties of the beam. A more likely explanation is that these particles have been scattered somewhere along its trajectory, and since the chip itself was placed inside a vacuum chamber, it is reasonable to assume that the scattering most likely occurred on top of the chip layer. This would also explain why the purple areas are relatively close to the beam pattern as scattered particles from the top layer would not have been able to travel far since the vertical distance to the epitaxial layer is so small. The opposite would occur if the particles scattered earlier in the air, where even a small angle deviation from its original trajectory could lead to a particle hitting relatively far away from the center.

The blue and light blue region are pixels that are outside the beam spots but are fired due to the diffusion process of the charge carriers. This explains the round shape, which occurs because the charge carries will on average diffuse equally in all directions. The green, yellow and red regions are pixels that are close to or inside the beam scanning pattern and received the most hits.

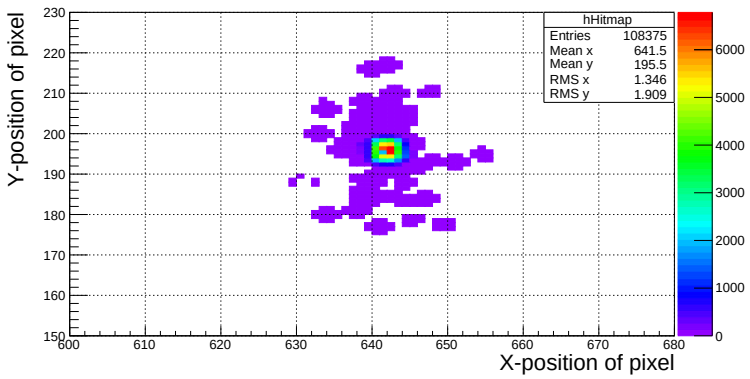

Figure 5.8: Raw hitmap of a 128×128 μm^2 scan with V_{bb} = -3 V.

Figure 5.8, which is the same run but with a V_{bb} = -3 V, have the same trend. The main difference is that the number of firing pixels is much lower since an increase of the back bias voltage makes the charge carriers diffuse less. The purple area is now split into single clusters since the charge carriers were unable to spread to a nearby region which also received hits.

5.3.2 Single Clusters

A Helium-4 ion with an energy of 10 MeV will deposit approximately 2 MeV inside the 25 μm thick silicon epitaxial layer of the ALPIDE [8]. Such high energy deposition will create an electron cloud capable of diffusing to many pixels. With a back bias voltage equal to 0 V, the only voltage present is the electrical field generated by the p-n junction on top of the epitaxial layer of the pixel. This setting allows the electrons to drift far before the n-diode collects them because the electrical field is low and the depletion zone itself is small. The following figures show two examples of single clusters captured with the same parameters.

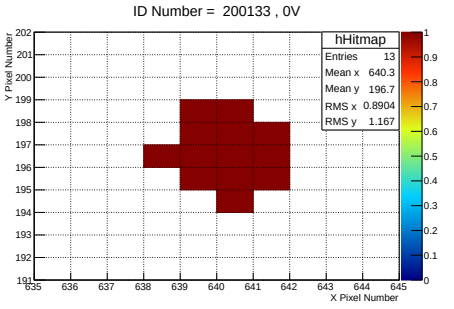

Figure 5.9: Single small cluster on the chip at $V_{bb} = 0$ V.

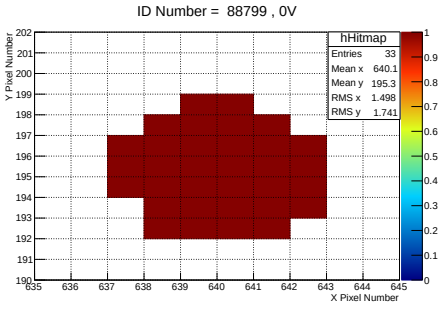

Figure 5.10: Single big cluster on the chip at $V_{bb} = 0$ V.

As seen in figure 5.9 and 5.10, the clusters have a different form and size. The cluster in the left figure has 13 firing pixels, while the one to the right has 33 firing pixels. From these two clusters, one can already observe that the cluster size varies from 13 to 33, even though the parameters are kept the same. The only thing that differs from these clusters is the time in which they were registered, seen by their event ID differences. These clusters have, therefore, originated from two distinct helium particles. The cluster size variation could, therefore, come from Landau fluctuations, meaning that the particles deposited a different amount of energy in the chip due to the random variation of the number of collisions occurring in the thin epitaxial layer. Another explanation is that the sizes of the clusters are connected with the beam spot position. As the particles hit the detector at separate times, and hence different places, this could indicate that the cluster sizes also depends on the locations of the deposited energy.

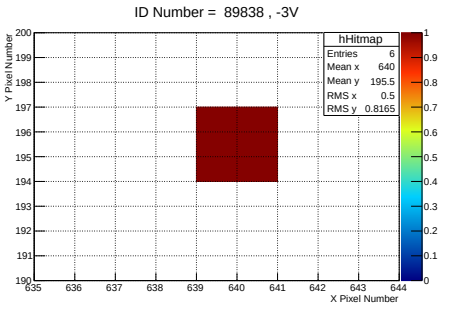

Figure 5.11: Single small cluster on the chip at $V_{bb} = -3$ V.

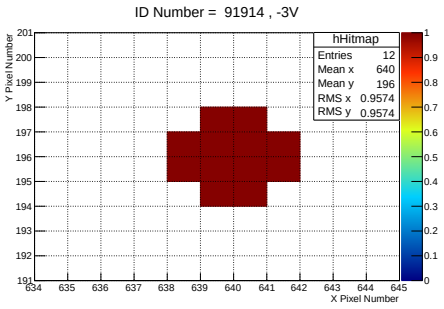

Figure 5.12: Single big cluster on the chip at $V_{bb} = -3$ V.

Figure 5.11 and 5.12 are clusters captured with $V_{bb} = -3$ V. With this back bias voltage, the charge carries diffuse less than for the 0 V configuration, and hence,

the clusters are smaller. This is because, as mentioned in chapter 3.3.1, the applied electric field increases the volume of the depletion region under the n-well diode. This effect reduces the diffusion capability of the charge carriers as they have a higher chance of diffusing to the depletion region than before.

5.3.3 Consecutive clusters

Recent studies have shown that the cluster from an alpha particle in the ALPIDE chip has a time over threshold period of around 5-8 μs [21]. This means that with a trigger period of 10 μs there is a high chance of sampling the same cluster twice in two consecutive triggers. These successive frames will have an ID number difference of one.

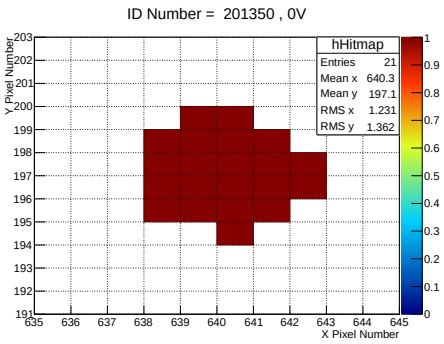

Figure 5.13: First frame of a double consecutive cluster (ID number = 201350).

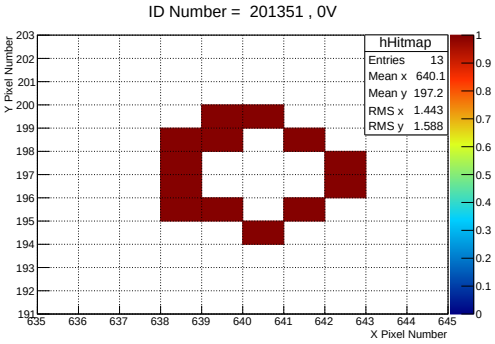

Figure 5.14: Second frame of a double consecutive cluster ID number = 201351).

In figure 5.13 and 5.14, the two clusters came from the same helium ion, but the signal duration was long enough to be captured in two consecutive triggers. As seen in the figures, the last frame of the cluster is less in size and only consist of pixels in the periphery of the cluster. This comes from the diffusion process discussed at the beginning of this chapter, that the pixels in the boundary of the cluster will collect the charge at a later time. Therefore, there is a chance that these pixels will fire again after the center pulse charge has vanished. This creates a cluster with a doughnut shape (figure to the right), which is the shape often observed in the last frame of a cluster sampled twice.

There is, as discussed in section 5.1.1, another type of development seen in the clusters. The pixels closest to the deposited charge will receive charge carriers first and be triggered earlier than the pixels further away. Therefore, if the trigger comes early in a cluster development, only the pixels closest to the deposited charge will show a hit, and the pixels further away will get fired later at the second trigger. In

those consecutive frames, the charge carriers have had insufficient time to developed entirely by diffusion, and the first frame contains fewer pixels than the last frame. An example is shown in figure 5.15 and 5.16.

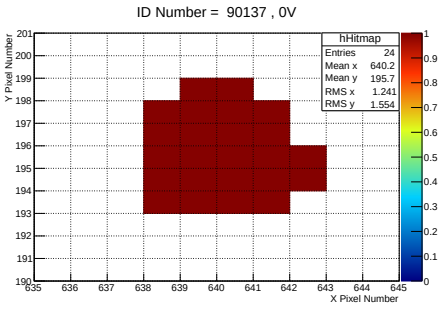

Figure 5.15: First frame of a double consecutive cluster (ID number = 90137).

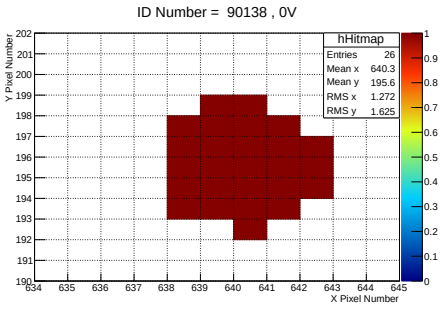

Figure 5.16: Second frame of a double consecutive cluster (ID number = 90138).

The cluster in figure 5.15 is sampled before it has developed completely, and in the second frame, figure 5.16, it has grown in size from 24 to 26 pixels.

This subsection shows that in order to find the correct sizes of clusters, one has to filter out those frames that only captures a part of a cluster. If, for example, all of the frames shown in figure 5.13 to 5.16 is included in the final result, there would be two wrong cluster sizes (too small). The cluster count, and hence particle count, would also be wrong, as there is only two distinct cluster, originated from two helium ions.

5.3.4 Fraction of consecutive frames

If the pulse charge of a cluster stays 5-8 μs over the time over threshold, and the trigger period is 10 μs, the number of consecutive frames containing the same cluster should be around 50 to 80 % (5-8 μs/10 μs). This can be checked by plotting the fraction of consecutive frames.

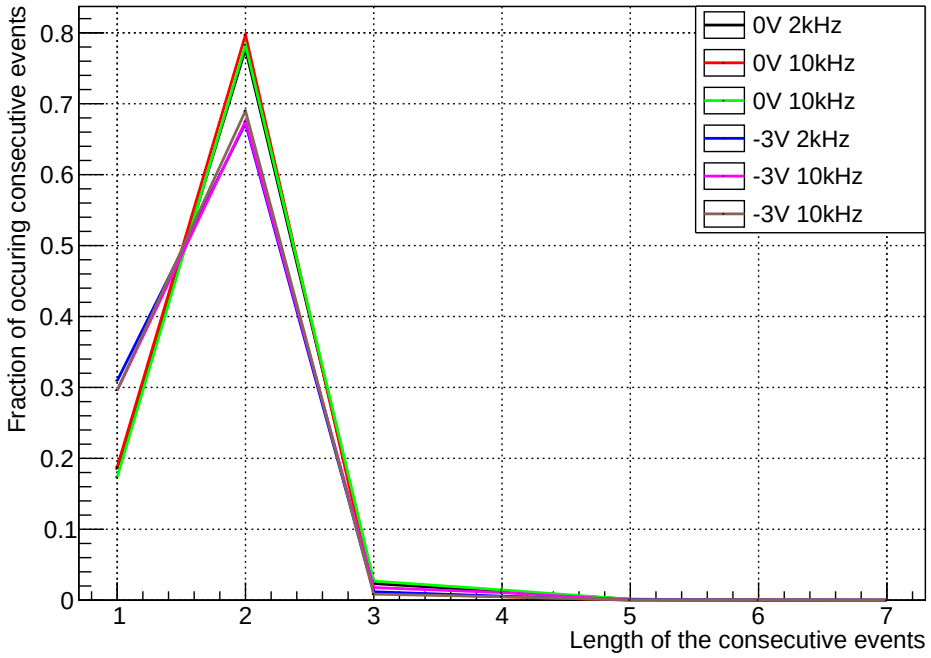

Figure 5.17: Fraction of consecutive events vs. length of the consecutive frames.

Figure 5.17 shows the fraction of consecutive frames for the all the runs used in this analysis. The 0 V runs (green, red and black line) has around 20% single frames and 80% double frames in the data set. This is as expected from the probability mentioned. The -3 V runs consists of 30% single frames and only 70% double consecutive frames (brown, purple and blue line). In these runs, the charge collection time is faster, and so the probability that a cluster is triggered twice is therefore less. The plot overall, in both cases, corresponds well statistically with the study regarding the time over threshold duration of a cluster [21]. It also highlights the importance of the post-processing step, in which these 70-80% double consecutive frames have to be corrected for in order to obtain the correct cluster sizes.

5.4 Results

An algorithm was implemented in c++ to deal with the consecutive frames. This algorithm would choose the biggest cluster if the cluster occurred in more than one frame. Another method was also tested, which took the union of the pixels occurring in the consecutive frames. However, taking the union of pixels occurring in consecutive frames can lead to a larger pixel count than any of the actual sizes, since consecutive frames could come from two particles hitting close in time. Therefore, the algorithm that chooses the biggest cluster was used in this analysis.

5.4.1 Cluster size histograms

If the size of the cluster only depended on the particle type, energy, and the chips configurations, the cluster size histograms should be Landau distributed. The figure 5.18 and 5.19 shows cluster size distributions for He-ion beam at 10 MeV with V_{bb}=0V.

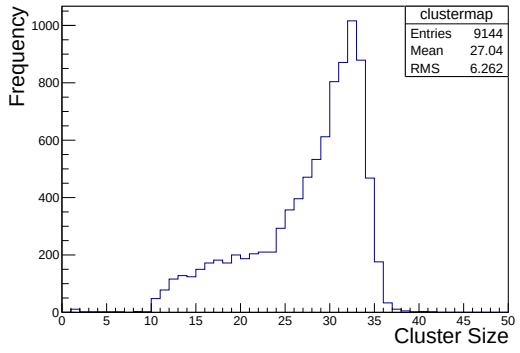

Figure 5.18: Cluster size histogram with beam rate at 2 kHz, dwell time of 100 ms and the chip at V_{bb} = 0 V.

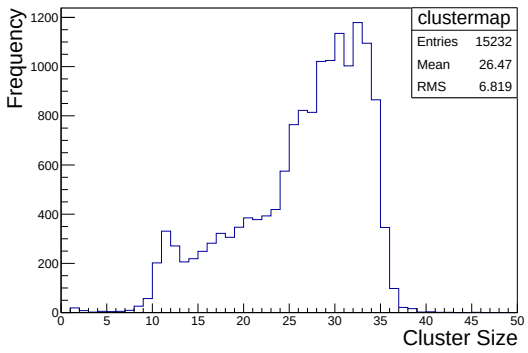

Figure 5.19: Cluster size histogram with the beam rate at 10 kHz, dwell time of 200 ms and the chip at V_{bb} = 0 V.

The distributions of the cluster sizes are broad. They both have a peak at roughly 32 pixels, but they also have a left tail containing clusters with fewer pixels. These smaller clusters are not underdeveloped as the algorithm specifically filter out such frames, and the 250 ns dead time in-between each strobe is too short to let any pixels firing go unnoticed. These histograms, therefore, represents the fully developed clusters and shows that the size of the clusters varies from around 10 to 35 in size as the beam position changed over the pixels of the ALPIDE.

In the following figures, the same beam parameters were used as in figure 5.20 and 5.21 respectively, but with reverse substrate bias at - 3 V.

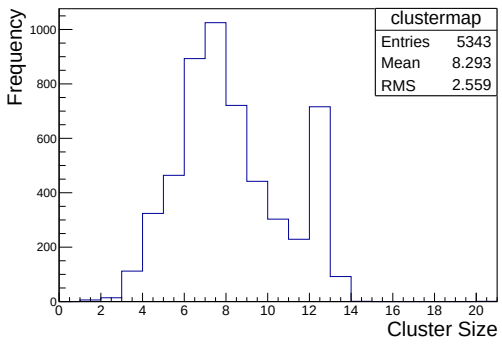

Figure 5.20: Cluster size histogram with the beam rate at 2 kHz, dwell time of 100 ms and for the chip at V_{bb} = -3 V.

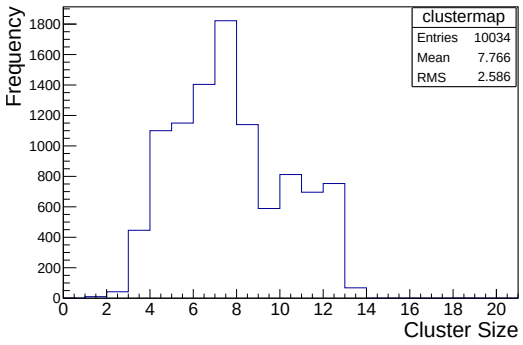

Figure 5.21: Cluster size histogram with the beam rate 10 kHz, dwell time of 200 ms and for the chip at V_{bb} = -3 V.

The histograms in figure 5.20 and 5.21 have the top peak at 7 pixels. However, the left histogram has another high peak of 12 pixels, while the right one has three large middle columns from 10 to 12. They both show that the cluster size distribution is broad and that there is a high amount of clusters with size 7, as well as larger clusters with size 10-12. These larger and smaller cluster size groups could come from the beam spot position and hence, the position of the incoming particle on the pixel. If the helium particle transverses the center of the pixel; there is a higher chance that more charge carriers diffuse to that pixel's diode than if the particle crossed the boundary of the pixel. Therefore, it could be that charge carries produced in the center of the pixel, diffuse less since a high number of them are collected by the first middle n-diode.

5.4.2 Cluster size vs. event ID

The main purpose of this experiment was to find out if there exists a correlation between the position of the deposited charge and the registered cluster size. As we have seen, previous plots showing the clusters and the cluster size histograms have already indicated that there is a broad distribution of the sizes in the clusters obtained. In order to investigate the position impact on the cluster size, one needs the find the beam position for the corresponding event.

The simplest solution to investigate the position of the beam versus the cluster size was, therefore, to plot the cluster sizes against the event numbers. As the event number and hence time increases, the beam position changes as it follows the scan procedure described in section 5.2.3. Such a plot is shown in figure 5.22 with an average of 300 events per point in order to observe the main features more clearly.

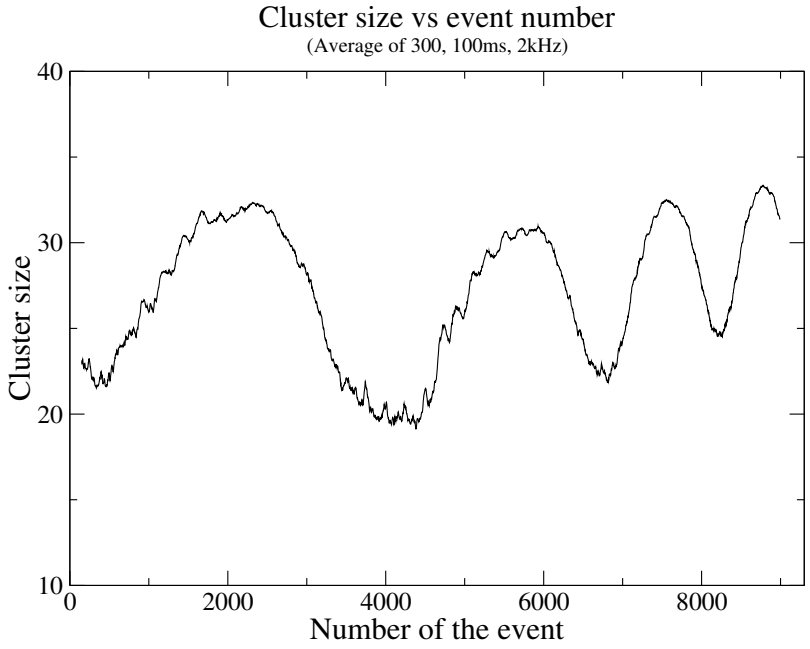

Figure 5.22: The cluster size vs. event number with an average of 300 events for each point.

From figure 5.22, one can see a clear oscillation of the cluster sizes. There are roughly four main whole periods in this oscillation, which corresponds well with the number of pixels scanned in the x-direction. It is important to remember that the pixels were scanned column by column, so the larger oscillations are due to the movement of the beam in the x-direction. Figure 5.22 shows that the cluster sizes have an average of roughly 20 pixels at some areas on the chip and an average size of above 30 in other areas.

Figure 5.23, however, also shows smaller oscillations on top of the main one.

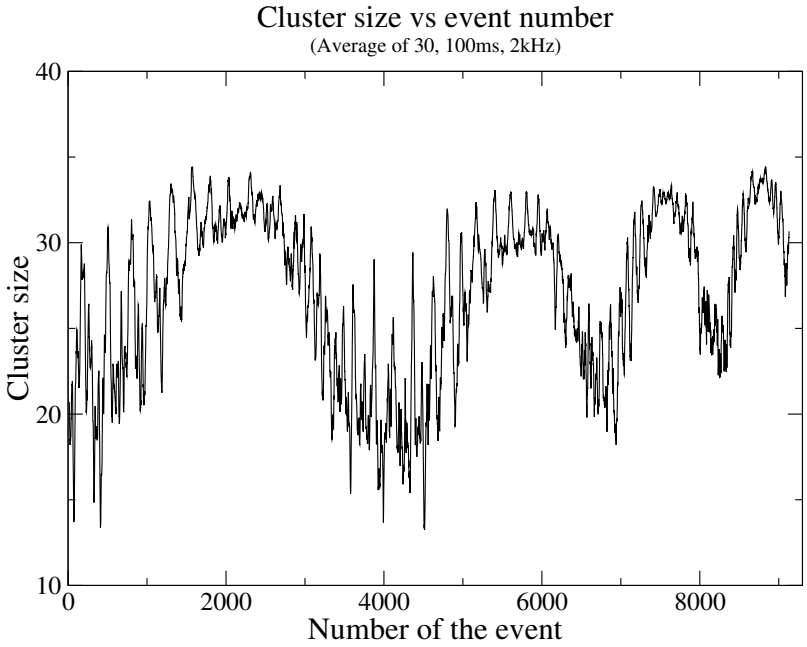

Figure 5.23: The cluster size vs. event number with an average of 30 events for each point.

This feature is more evident with an average cluster size of 30. This oscillation is likely to come from the change of the beam position in the x-direction, as the beam scanned roughly 4 pixels in this direction before it moved a step in the x-direction. These smaller oscillations, therefore, occur more frequently, but they also have an amplitude of approximately 5-10 pixels.

This means that within the large and a small oscillation, the average cluster size can change from roughly 15 pixels to 35 pixels, as shown in figure 5.23. These low and high regions, however, are only at specific beam spots, dependent on both the x and y-direction.

The same trend was also observed in the data with reverse back-bias of -3 V and also in the data which had the beam on longer dwell time and a higher frequency. Two of each example is shown in figure 5.24 and 5.25, respectively.

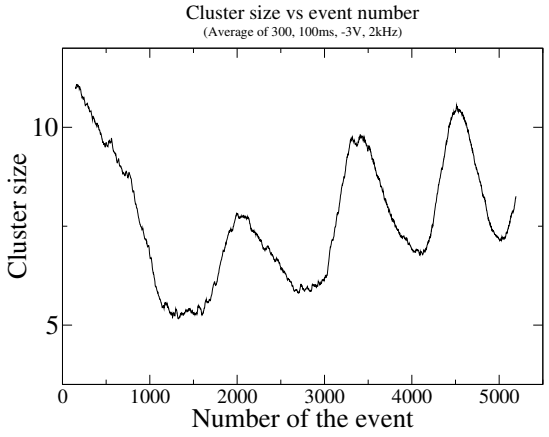

Figure 5.24: The cluster size vs. event number with an average of 300, with beam rate 2 kHz and dwell time at 100 ms for the chip at V_{bb} = -3 V.

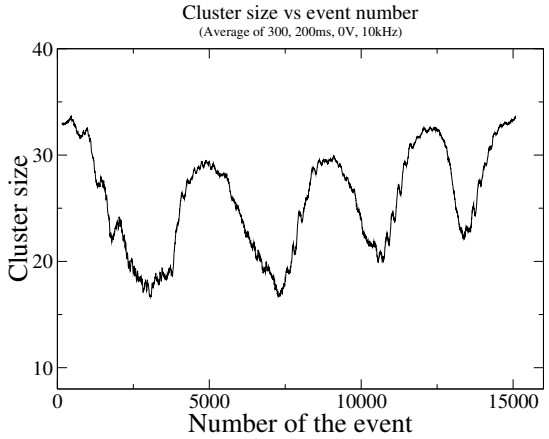

Figure 5.25: The cluster size vs. event number with an average of 300, with the beam rate 10 kHz, and dwell time at 200 ms for the beam at V_{bb} = -3 V.

The two last figures posted in this subsection also shows another less evident trend. Their last three top oscillation points tend to increase with time. This could come from the temperature increase with time caused by the irradiation of the helium beam. If the temperature increases inside the irradiated area of the chip, the charge carriers will diffuse faster and hence, result in larger clusters. Another possibility would be the radiation damage occurred at the pixel due to prolonged irradiation. The details of the radiation damage studies will be reported in one of the following sub-sections.

5.4.3 Cluster size vs. estimated beam position

A more challenging approach was developed in order to acquire information about the position of the beam and their associated events. In this method, the relative starting position of the beam, the scanning pattern and the dwell time of each beam spot were used. The first beam spot in each of the square scans always starts at the bottom left pixel and would move to a new spot every 100-200 ms, depending on the scan. One can, therefore, start with the bottom left spot and accumulate all the events hitting inside this dwell time period of 100 or 200 ms, and continue the process for all the following spots by using the pattern of the beam. When all the spots and their corresponding clusters have been acquired, one can plot the average cluster size for each beam spot position [1]. Such a 2D map is plotted in figure 5.26.

[1]The code is listed in the appendix

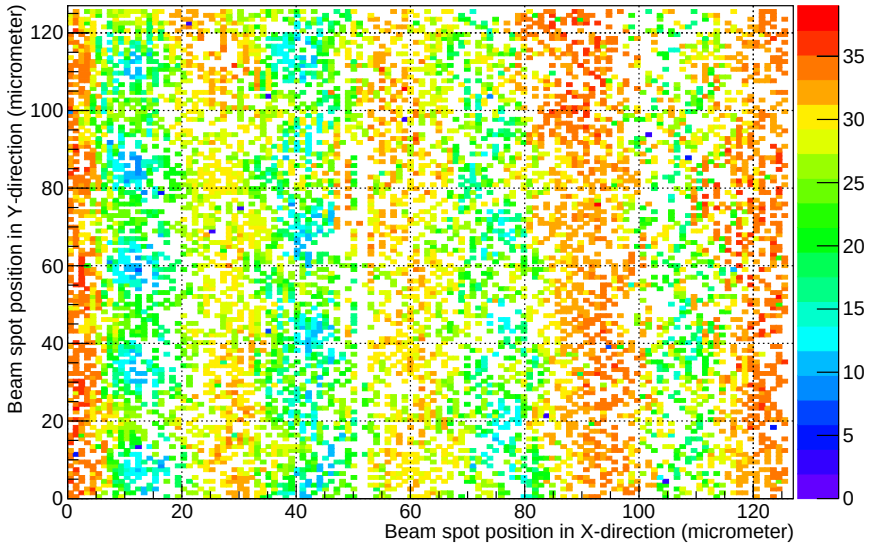

Figure 5.26: Average cluster size vs. beam position, with 200 ms dwell time, 10 kHz frequency and the back-bias voltage of the chip at 0 V.

The figure 5.26 is obtained for the 128×128 spots beam scanning with a beam frequency of 10 kHz and a dwell time of 200 ms. This beam frequency and dwell time gave the most statistics for each of the beam spots. In this figure, the cluster sizes show a clear dependence on the beam position. In the first 20 columns, the cluster sizes represented by the blue and light blue points, appear together in groups and these clusters have around 5-15 in size. These small clusters could come from the He-ions that transverses near or directly through the depletion zone. These charge carriers would be collected quickly by the n-diode and hence, would be able to diffuse less. This would also explain the grouped area observed on the figure as the depletion zone, seen from the top, is centered in the middle of each pixel.

The opposite would then occur when a particle transverses in the periphery of a pixel, and these induced charge carriers would be able to diffuse to a long distance away from the center of origin. These clusters could be the points shown as the yellow, orange, and red dots, as they appear furthest away from the blue areas and have sizes of roughly 30-35 pixels. The cluster sizes between these two extremes have sizes around 15-25 and are represented as the green dots. They appear between the assumed pixel centers.

Another suggestion is that the cluster size differences comes from the variations of the electrical circuits in the top layer of the chip. If this layer changes in thickness, then at some points the particle would be able to deposit more charge in the epitaxial layers than others.

The position correlation with the cluster sizes, however, disappears more as time

increases. At the end of the scan, between the 80 to 120 spots in the x-direction, the blue areas have vanished, and only large and middle large clusters are observed. This could come from the beam spot estimation, or from another effect like an increase in temperate or from radiation damage. These effects could possibly explain why the smaller clusters have disappeared at the end of the scan procedure.

The figure 5.27 and 5.28 shows similar plots made for the data taken at reverse back-bias voltage of -3 V, 100 ms dwell time and 2 kHz beam rate. The two plots can be looked at as the same plots but plotted in 1D and 2D.

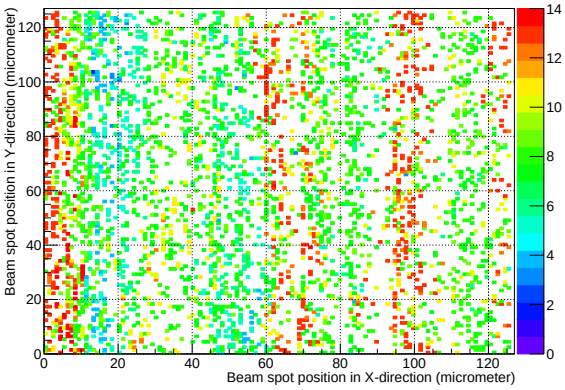

Figure 5.27: Average cluster size vs. beam position, with 100 ms dwell time, 2 kHz frequency and the back-bias voltage of the chip at -3 V.

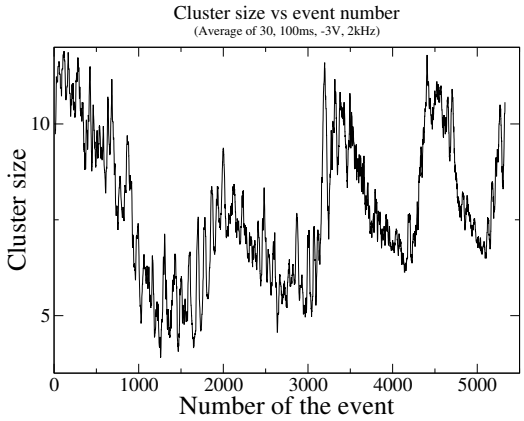

Figure 5.28: The cluster size vs. event number with an average of 30 events, with 100 ms dwell time, 2 kHz frequency and the back-bias voltage of the chip at -3 V.

The 2D figure at the left shows that the number of red column areas is four, and these column groups also appear in the right figure as four of the highest peaks. The yellow column between the 20 and 45 beam spot position in the x-direction in the left figure, is the smaller peak shown in the right figure between roughly the 1500 - 3000 event number. This clear correlation between the different plotting methods indicates that the more challenging 2D approach was done more or less correctly. However, the 2D map in figure 5.27 does only have a correlation between the x-direction of the beam spot and the cluster size. This could come from an inaccuracy of the beam spot estimation, or that the statistics for each beam spot is too low for the 100 ms dwell time data to observers any differences in the y-direction.

5.4.4 Radiation damage effects

After the ANSTO experiment, the threshold and noise were measured to look for radiation damage. These measurements were conducted together with M.Sc. Susmita

Afroz at the University of Bergen [25].

If the chip would have been damaged by the helium beam, the scanned areas should have a lower charge threshold and a higher noise than the unscanned regions. Figure 5.29 shows the results from the threshold measurement from the chip at V_{bb} = -6 V. This charge threshold map was obtained by injecting different charges into each pixel in multiple steps and then plotting the electron value at which the pixel fired.

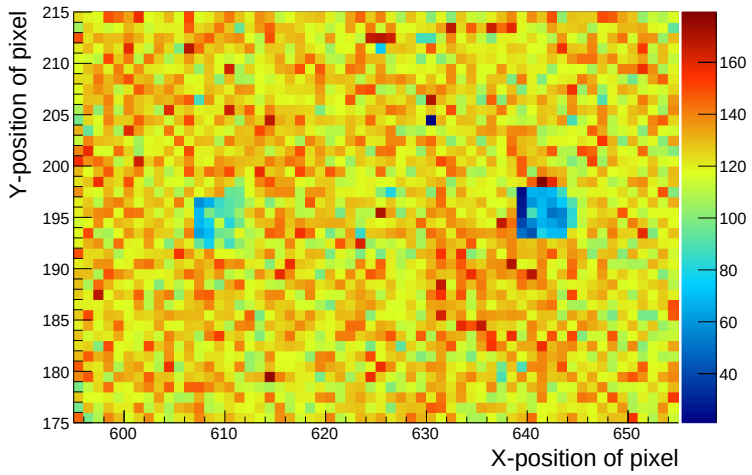

Figure 5.29: Threshold map after irradiation for the two scanned square areas with V_{bb} = -6 V.

The light blue region to the left in the figure represents the area which was scanned with the beam at 2 kHz rate and dwell time of 100 ms. This area has a slightly decrease in threshold value, around 60-90 electrons, compared to the surrounding unscanned areas which have 100 electrons and above. The blue area to the right, however, was scanned with 10 kHz beam rate with a 200 ms dwell time. This area has been exposed to a larger amount of dose compared to the other scan, and have, therefore, a clear decrease in the threshold of about 30-60 electrons.

Figure 5.30 shows the noise measurements at V_{bb} = -6 V.

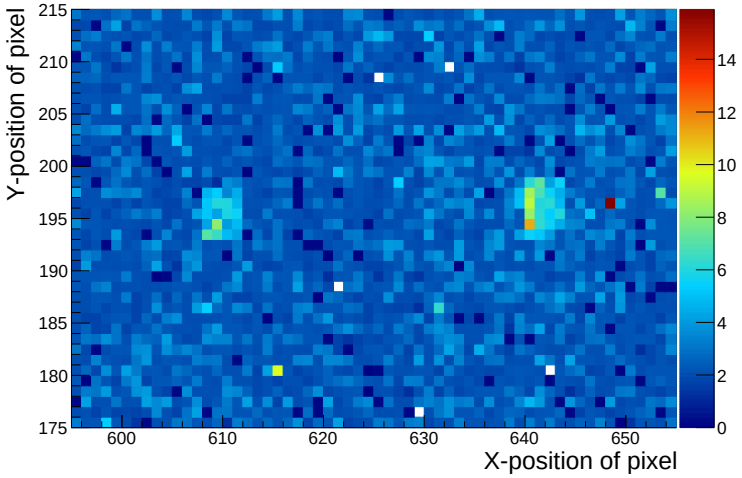

Figure 5.30: Noise map after irradiation for the two scanned square areas with V_{bb} = -6 V.

In this figure, the two scanned areas have the same position as in the threshold map. In this map, the noise of the left region and right region has increased. The right region is still more affected as the beam dose was as mentioned higher in this scan. The noise is also given in electron values, and for the irradiated areas, the noise has increased by roughly 4 electrons.

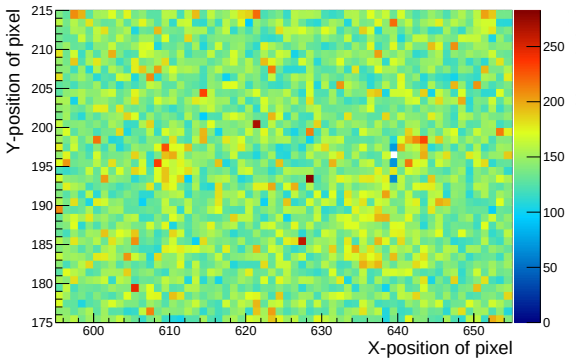

Figure 5.31: Threshold map after irradiation for the two scanned square areas but taken with V_{bb} = 0 V. The vision of the two areas are gone as there is almost no difference.

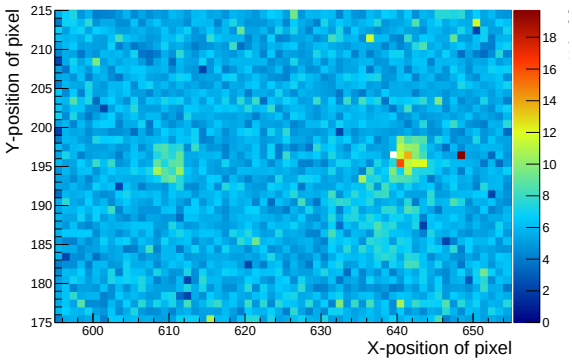

Figure 5.32: Noise map after irradiation for the two scanned square areas with V_{bb} = 0 V.

Figure 5.31 is the threshold map obtained on the chip at V_{bb} = 0 V. In this plot, the difference between the threshold values for the scanned and unscanned regions are substantially small, making it difficult to see the regions. There are three pixels in the threshold map at the area to the right which have a blue or dark blue color, meaning that their threshold values have decreased roughly 50-60 electrons compared to the surrounding green-yellow areas. In figure 5.32, however, which is the noise map obtained with V_{bb} = 0 V, the two irradiated areas is still noticeably separated from the surrounding pixels. The noise in the left area has increased with around 3 electrons and in the right area, about 4-5 electrons.

The dose was estimated by using the number of spots, dwell time and the beam frequency, as well as the ASTAR tables for 10 MeV helium ions in silicon. These dose calculated for the region to the left was approximately 15 kGy and 32 kGy for the right region. The radiation effects in the noise and threshold measurements are, therefore, more evident for the right area, as those pixels has received a dose which is more than double as high compared to the pixels in the left area.

The decrease in threshold values and the increase in noise could be part of the reason why the cluster sizes gradually increase with time. For a lower threshold value, the pixels would need less charge to get fired, and the same argument is valid for a noise increase. Hence, larger clusters could appear more frequently at the end of the scan procedure due to a gradual increase of radiation-induced effects with time.

However, the threshold map only showed clear differences at V_{bb} = -6 V between the scanned and the unscanned regions, and the experiment at ANSTO was conducted with V_{bb} = 0 V and -3 V. The radiation damage effects are, therefore, not a likely explanation of the main cause which lead to a cluster size increase during the measurements at the ANSTO facility.

5.4.5 Temperature effects

As the chip in the ANSTO experiment was placed inside a vacuum chamber, there would be no thermal conduction between the chip and the environment. The chip would, hence, increase in temperature when irradiated with helium beams. Therefore, a second experiment was conducted after the ANSTO experiment to study the correlation between the temperature of the chip and the cluster sizes.

The temperature conditions were controlled by placing the ALPIDE chip and the DAQ board inside an insulated chamber, as shown in figure 5.33.

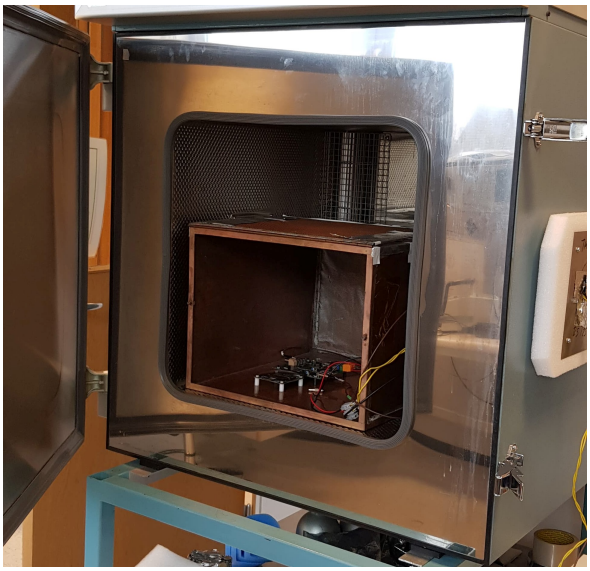

Figure 5.33: The setup of the temperature measurement, showing the ALPIDE chip placed inside the insulated chamber. The chamber changed temperature by using cooled or heated airflow.

The chip was irradiated with a ^{241}Am source. The trigger and strobe length were set to 500 μs and 485 μs, respectively. By having a longer strobe, the deadtime would decrease, and since the intensity of the source was relatively low, the probability of getting two hits within the same position would remain small. The deadtime between each trigger was then 15 μs, and since the total charge of a cluster stays 5-10 μs, it was impossible for an induced signal to be captured by two successive strobes. This resulted in no double consecutive clusters observed in the data. The measurements were conducted within a temperature interval from 15 to 40°C, with 5°C steps. These measurements were conducted twice, with a back bias voltage at 0 V and -3 V, respectively.

An example of two of the recorded cluster distributions at 15°C is shown in figure 6.8 and 5.35 for V_{bb} = 0 V and -3 V, respectively.

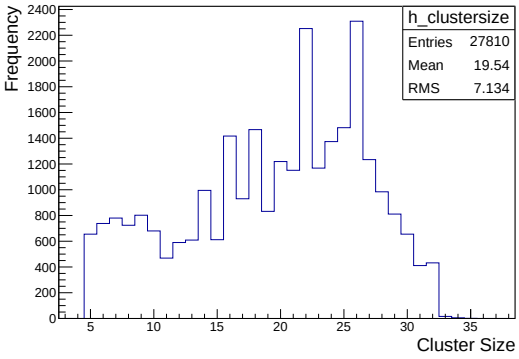

Figure 5.34: Cluster size distribution for a ^{241}Am source at 15°C with $V_{bb} = 0$ V.

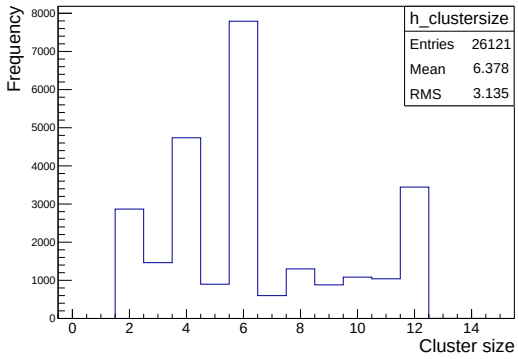

Figure 5.35: Cluster size distribution for a ^{241}Am source at 15°C with V_{bb} = -3 V.

In the plot reported on figure 5.34, the clusters with sizes smaller than 4 pixels were cut out due to noisy pixels which made a high occupancy of smaller clusters. For the plot in figure 5.35 clusters with sizes smaller than 1 pixel were cut out, for the same reason. The mean of these distributions was calculated for each temperature step, as well as the RMS of the mean (sample standard deviation) defined as:

$$s = \sqrt{\frac{\sum_{i=1}^{N}(x_i - \overline{x})^2}{n-1}}, \tag{5.1}$$

where $\{x_1, x_2, ..., x_N\}$ are the observed values, $\bar{x}$ is the mean value of these observations, and n is the number of observations. The error is then evaluated as the standard error of the mean:

$$SE_{\mu_x} = \frac{s}{\sqrt{n}}. \tag{5.2}$$

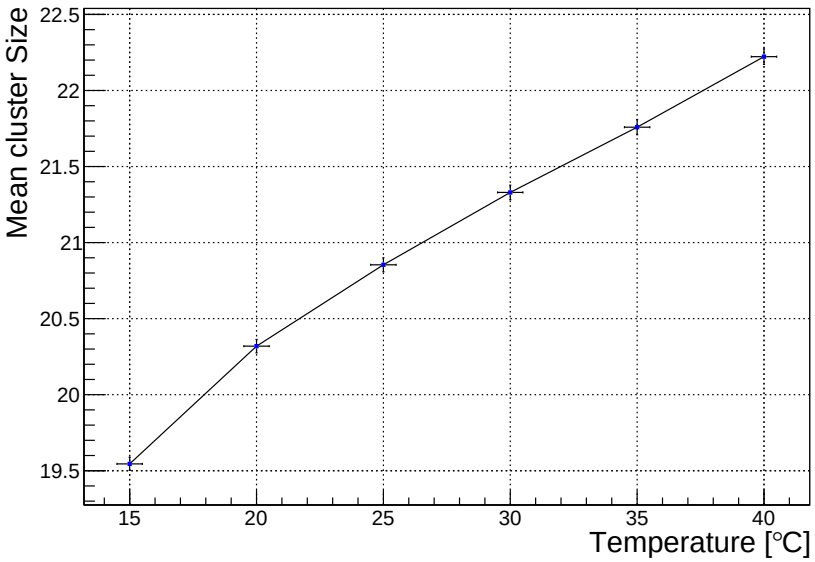

Figure 5.36: Mean cluster size vs. temperature for irradiations with $V_{bb} = 0$ V.

Figure 5.36 shows the mean cluster size measured at temperatures between 15 and 40°C. The plot shows that the average cluster size increases gradually with increasing temperature. Above 25°C, the increase looks linear w.r.t. the temperature.

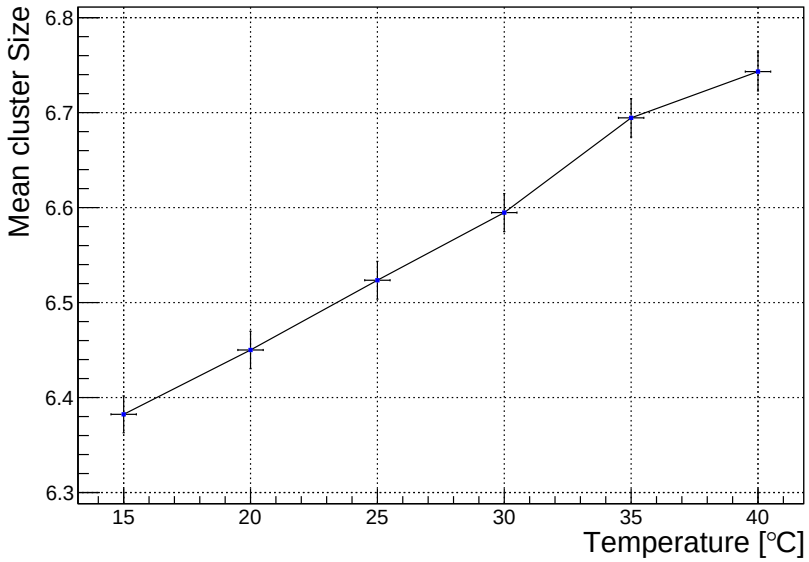

Figure 5.37: Mean cluster size vs. temperature for irradiations with V_{bb} = -3 V.

The same results were also obtained for the measurements with V_{bb} = -3 V. These results are shown in figure 5.37. In this case, the cluster size increased as the temperature was raised, but at a much smaller rate. The mean of the cluster size increased of about 0.35 pixels from 15 to 40°C.

The reason behind these results is that the mobility of charge carriers is dependent on the temperature of the medium. When the temperature increases, the mobility increases as well, and hence, electrons diffuse faster, leading to larger clusters. At the ANSTO facility, the helium beam deposited on the pixels a dose equal to 15 kGy and 32 kGy. This dose leads to a temperature increase which can be estimated by using the specific heat of silicon. The temperature increase of the pixels was then estimated to be roughly Δ21°C for the 15 kGy dose area and Δ45°C for the 32 kGy area [2]. As the temperature measurements conducted at the UiB showed that there is a clear clusters size increase above 25°C when V_{bb} = 0 V, this indicates that the temperature variation during the helium scan would contribute to the gradual cluster size increase observed at the ANSTO experiment.

[2]This is only a rough estimate as it does not include the thermal conductivity between the irradiated pixels and rest of the chip, and the actual temperature increase of the pixels would, therefore, have been lower.

CHAPTER 6

Characterization of the ALPIDE Telescope

This chapter presents the experiment conducted at the Heidelberg Ion-Beam Therapy Center (HIT) in July 2018. The parameters of helium and proton beams are outlined here, together with the configuration and placement of the chips. In the end, the results are presented.

6.1 Experimental setup

The purpose of the experiment was to study the clusters originating from helium ion and proton tracks at different energies and to measure the tracking efficiency for these particles. This was done by using three ALPIDE chips stacked together, as shown in figure 6.1. The chips were placed inside a mechanical stand made at the University of Bergen. The HIT facility beam then irradiated the chip with clinical energies and intensities.

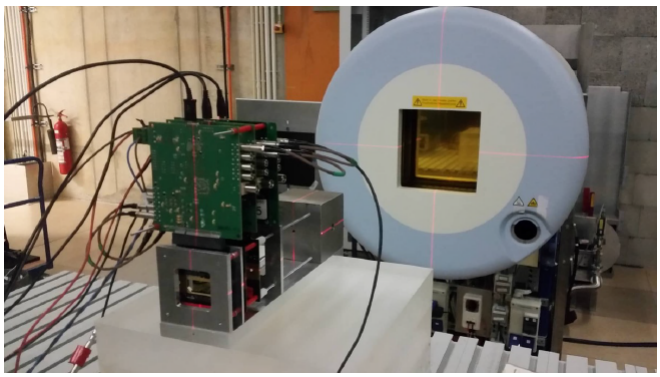

Figure 6.1: Picture of the overall setup at the HIT experimental hall, showing the ALPIDE stand and the beam exit.

6.1.1 Beam specifications

The HIT facility provides Helium-4 ion and proton beams at clinical energies and intensities. For the described experiment, the beam had an extraction time of 12 s and delivered intensities from around 10^5 to 10^6 particles per second. The energies used, together with their Full Width at Half Maximum (FWHM) is provided in the table 6.1 below.

Table 6.1: Table of the energies and their respective FWHM for helium ions and protons.

Helium Ions		Protons	
Energy in MeV/n	FWHM in mm	Energy in MeV	FWHM in mm
220.5	10.1	221.06	12.6
200.38	10.2	200.11	12.8
150.11	11.1	48.12	32.7
100.19	12.9		
50.57	20.6		

These helium and proton energy steps were chosen to look at the tracking efficiency at different energies and to look for a cluster size vs. energy correlation. To study the performances of the ALPIDE chips and the readout electronics, the beam frequency was set as low as possible. However, the online monitoring chambers at HIT are optimized for the high-frequency particle rate used in particle therapy, therefore below a certain threshold, the beam becomes invisible to them. For this reason, an additional scintillator was used, and it gave a rough estimate of the frequency which was around 100 ± 50 kHz at these energies.

6.1.2 The ALPIDE stand

A mechanical stand was constructed at the University of Bergen to allow the chips to be stacked closely together. The stand was made out of aluminum, and four long screws connected the front and back aluminum plate. Figure 6.2 shows the drawing of the mechanical stand.

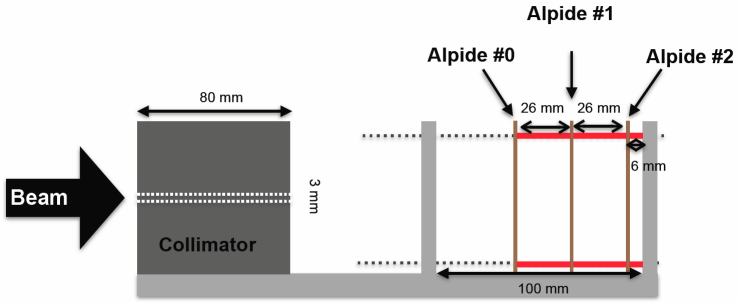

Figure 6.2: Schematic drawing of the mechanical stand and the three chips placed within it.

As shown in figure 6.2, the three chips were placed within the stand and were kept aligned by using four long screws that went from the front to the end aluminum plate. In this setup, the chips are referred to as DUT0 for the first chip, DUT1 for the middle chip and DUT2 for the last chip (Device Under Test). The gap between each chip was 26 mm, and the gap between DUT2 and the end aluminum plate was 6 mm. The DAQ boards were placed directly on top of these chips by simply using the connection as support. A steel collimator was also made in order to protect the readout electronics around the chip from radiation. The collimator was $8\times8\times8$ cm^3 in size with a 3 mm in diameter hole in the middle. The stand is shown in figure 6.3 together with the chips and the connections.

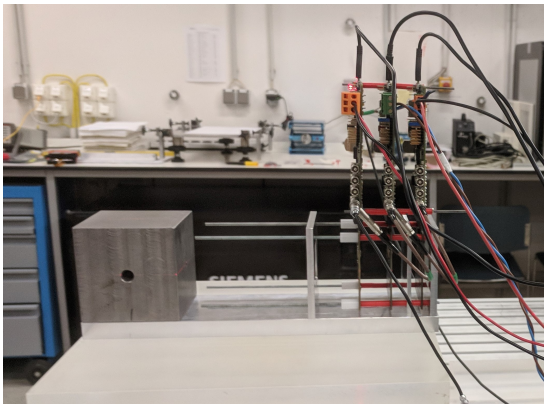

Figure 6.3: The ALPIDE telescope viewed from the side.

The ALPIDE telescope was placed on a movable bench and faced towards the beam exit. The bench could be moved in all directions which were beneficial for aligning the setup directly in front of the beam exit. Lasers in the experimental hall were

used for this alignment, and the chips were placed in the beam line in a way such that the center of the first chip from the beam point of view was at the isocenter as shown in figure 6.4.

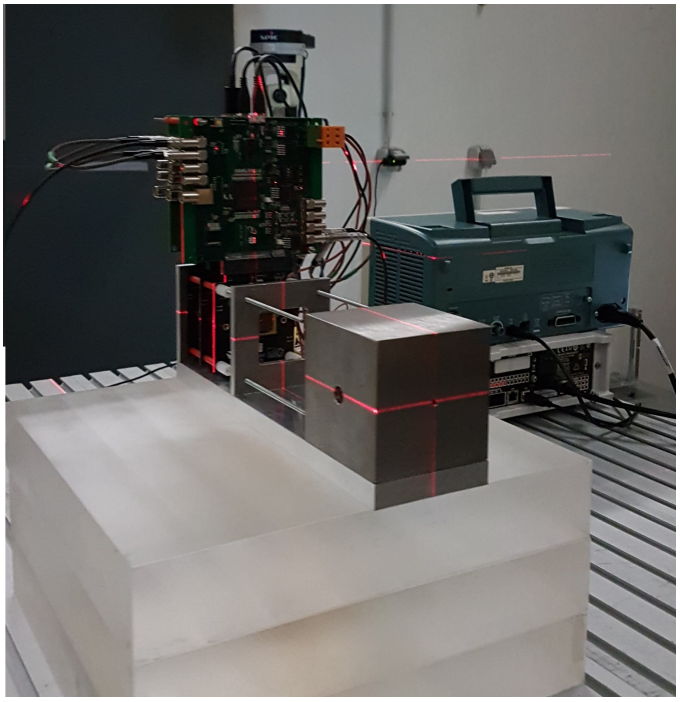

Figure 6.4: The setup of the ALPIDE chips aligned with the lasers.

6.1.3 The ALPIDE settings

The settings of the ALPIDE was kept the same as for the Bergen and Australia experiments, except that the reverse back-bias voltage was set to $V_{bb} = 0$ V for all the runs. The trigger period was set to 10 μs with a 9.75 μs strobe duration.

6.2 Results

The Data Acquisition (DAQ) tool used in this experiment was EUDAQ, a generic data acquisition framework developed by the International Linear Collider (ILC) community for detector applications [26]. This tool converted the data into a specific format which could be analyzed with EUTelescope, a software created as a consistent chain to EUDAQ for data analysis.

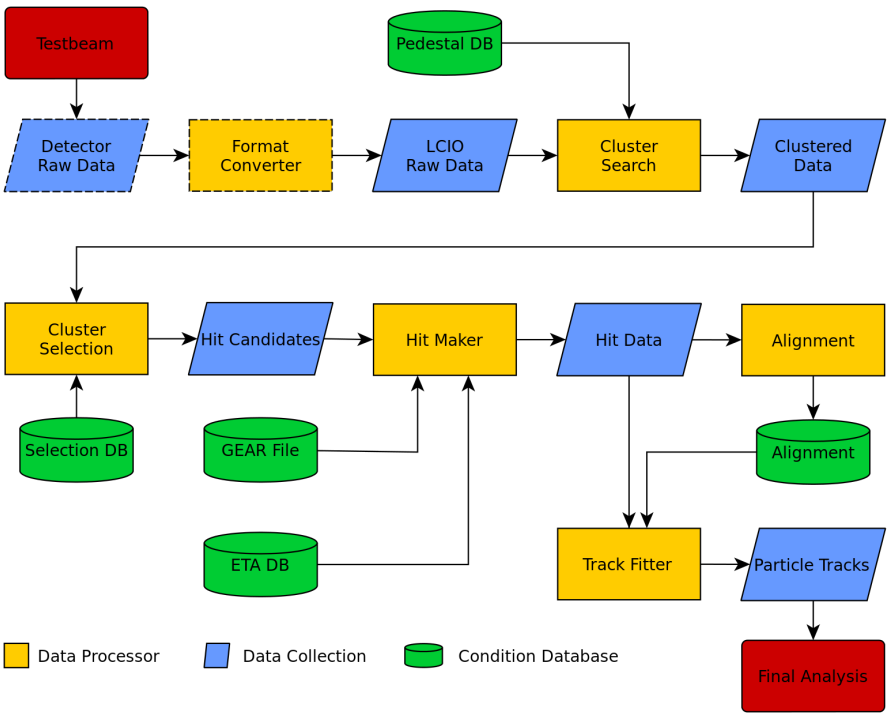

Figure 6.5: The EUTelescope framework [26].

Figure 6.5 illustrates the components of the EUTelescope framework. The raw data is collected by the EUDAQ tool and converted into LCIO (Linear Collider I/O) format readable by the EUTelescope. The analysis software finds all the clusters but only select those fulfilling the conditions set by the user. The CoG of these clusters are used as hit candidates for software alignment and particle tracking [1]. However, the EUTelescope in its original release lacks the ability to filter out those clusters which are read out twice. Therefore, the results shown in the following subsections concern the study of the energy vs. cluster size for helium ions, as the tracking results would be incomplete without this correction. Also, it followed that the cluster distributions obtained from EUTelescope in these results contained all clusters and not only those clusters belonging to a track.

[1] In the alignment step, the software fits straight tracks through the hit points and stores the offset of each detector layer. Before every set of runs, a high energy run was taken for this alignment step in order to provide the software with the straightest tracks.

6.2.1 Hit map of the beam profile

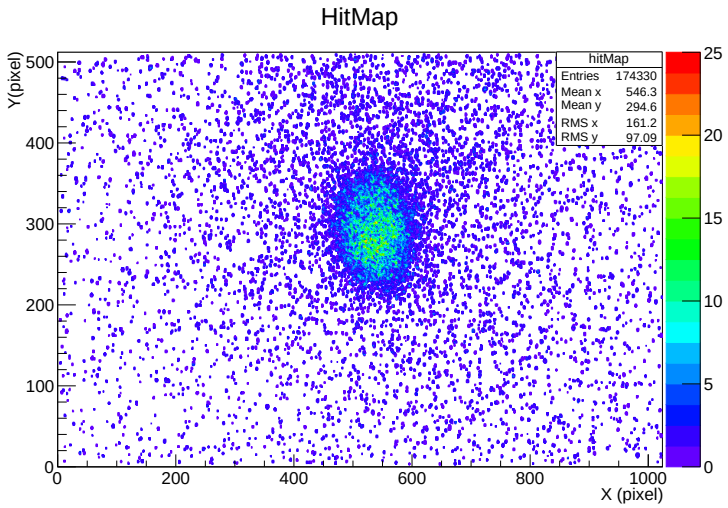

Figure 6.6: Hit map of the 220 MeV/n helium energy data showing the beam profile in DUT0.

Figure 6.6 is a raw hit map of the first chip from the beam point of view irradiated with the helium beam at 220 MeV/n. This hit map shows all the pixels that were fired during the run, producing an image of the beam profile. The image shows a densely hit area in the middle of the chip, and this is a good indication that the telescope was properly aligned along the beam direction leading to the beam hitting the center of the chip. The green and blue dense area also cover roughly 100-120 pixels in the x and y-direction, corresponding to a circular area of 3-3.2 mm diameter, while the hit occupancy decreases rapidly in all directions away from this center. This indicates that the collimator effectively reduces the intensity outside its 3 mm range since without the collimator the FWHM of the beam profile should be 10.1 mm.

However, figure 6.6 also shows pixels firing over the whole chip, including pixels on the edge. This spreading effect is mostly due to multiple Coulomb scattering (MCS) affecting helium ions crossing air or the downstream edge of the collimator aperture. Additionally, this effect can be produced by secondary particles or helium fragments, which can be created by nuclear interactions of the primary ions with the collimator material. If fragments and secondaries are created, again, at the downstream edge of the collimator aperture, they can have the necessary energy to reach the ALPIDE chip.

6.2.2 Consecutive clusters

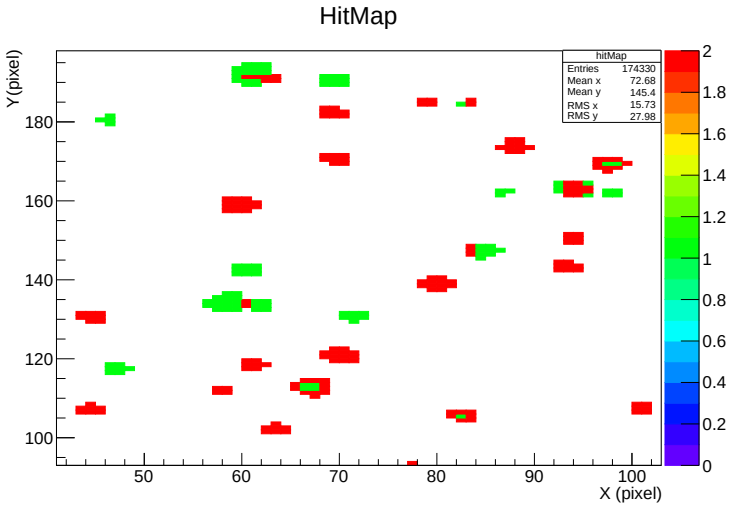

Figure 6.7: Hit map at the edge of the chip.

Figure 6.7 is the same hit map but zooming in on the hits occurring at the bottom left edge of the chip. The green pixels have recorded one hit, while the red pixels have recorded two hits. As discussed in subsection 5.3.3, due to the small dead time between each trigger, a charge signal produced in a pixel has the ability to occur in two consecutive frames. This is why most of these pixels show two hits even though they were only hit once by a single particle [2].

The EUTelescope software in the present release will include all such double firing clusters into the analysis. This would lead to a wrong cluster size distribution, as the clusters would be sampled randomly and could appear in any of their development stages. However, the EUTelescope separately stores empty middle clusters (doughnut-shape clusters) into its own cluster size distribution. Since these clusters are all roughly in the same development stage, they can be used to study the cluster size energy dependency. The doughnut-shaped clusters were, therefore, used in the following analysis. Though the cluster size distributions are all biased to lower pixel numbers as they are missing a pixel or pixels in the center, the correlation between the cluster size and the beam energy should still be valid.

[2]The red pixels at X = 60 and Y = 135 appears to come from two separate clusters which overlapped.

6.2.3 Cluster size distributions

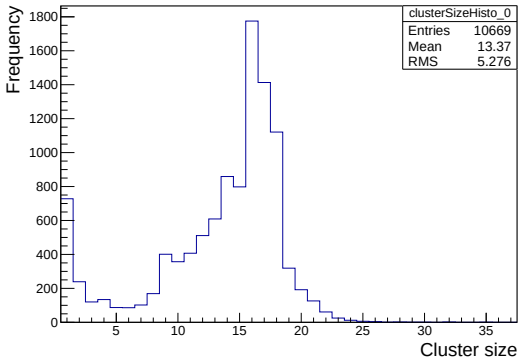

Figure 6.8: Cluster size distribution for a 50 MeV/n helium run on DUT1 without the correction of the double firing pixels.

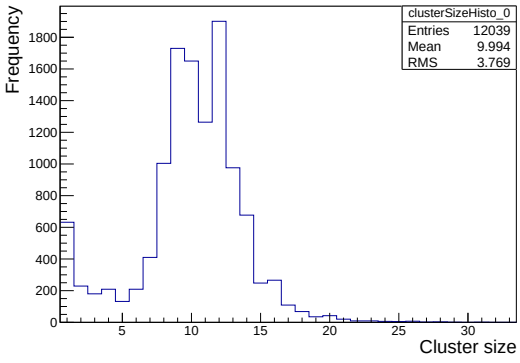

Figure 6.9: Cluster size distribution for a 150 MeV/n helium run on DUT1 without the correction of the double firing pixels.

Figure 6.8 and figure 6.9 are two examples of the cluster size distribution and show the distributions for the 50 and 150 MeV/n helium runs, respectively. These distributions were obtained by plotting all the clusters occurring on DUT1. The figure on the left, has a clear high peak around 17 pixels, with a tail of smaller cluster with a size from 15 to 5. A smaller peak is also visible on the left, with clusters containing only 1 pixel. The figure on the right has two high peaks occurring at 9 pixels and 12 pixels, and it also has a smaller peak with clusters containing a single pixel on the left.

It is likely that many of those smaller clusters with size of 1 to 3 pixels are clusters read out twice by two consecutive triggers. The charge signal of the helium particle would then had been able to leap over two successive strobes, and hence, some of the few pixels which still had leftover charge could have been read out. This would lead to a higher chance of sampling smaller cluster sizes.

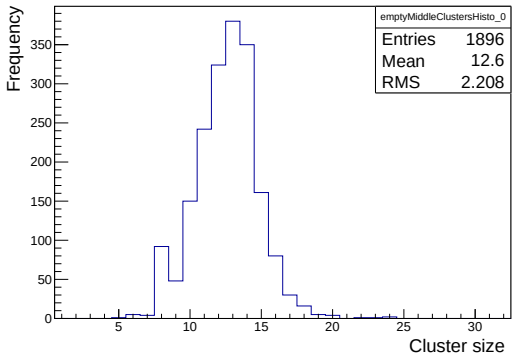

Figure 6.10: Cluster size distribution for a 50 MeV/n helium run on DUT1 for the empty middle clusters.

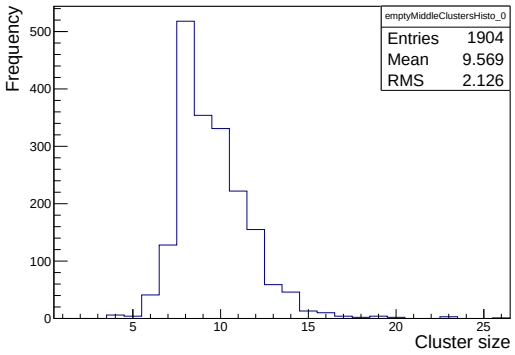

Figure 6.11: Cluster size distribution for a 150 MeV/n helium run on DUT1 for the empty middle clusters.

Figure 6.10 and 6.11 are the cluster size distributions of doughnut-shaped clusters for the same runs described above. As opposed to the previous plots, these distributions have no clusters smaller than 3 pixels, and their distributions look more confined. This is because the doughnut-shaped clusters are fully developed, and hence, their distribution does not contain those clusters read out too early or too late in their development stage.

The plot shown on figure 6.10 (50 MeV/n) looks almost Gaussian, but that on figure 6.11 (150 MeV/n) has a Landau distribution. The same difference can be seen when plotting the distributions obtained for the 100 MeV/n and the 220 MeV/n helium runs shown in figure 6.12 and 6.13, respectively.

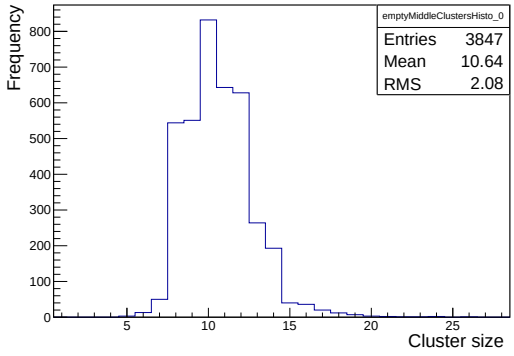

Figure 6.12: Cluster size distribution for 100 MeV/n helium run on DUT1 for the empty middle clusters.

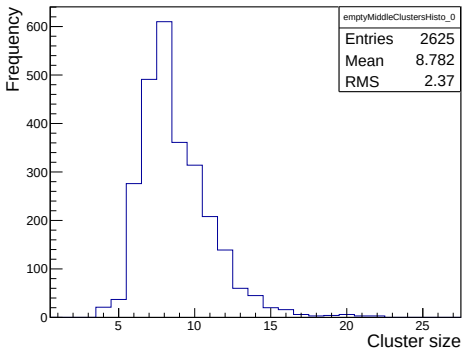

Figure 6.13: Cluster size distribution for 220 MeV/n helium run on DUT1 for the empty middle clusters.

From these four plots, it can be seen that as the energy increases, the distribution goes from having a Gaussian shape towards a Landau shape. This could be explained by the number of collisions that the helium particle undergoes in the chip layer at different energies. When the helium particle has a high energy, the distributions is best described as the energy loss for an ionizing particle in a thin absorber, and this has a Landau distribution. However, as the energy decreases, helium ion experiences more and more collisions, and the Landau distribution valid at small number of individual collisions, becomes more a Gaussian distribution.

6.2.4 Cluster size vs. energy

From the plots shown in the previous subsection, it can be seen that the mean of the cluster size distribution increases as the energy of the helium ion decreases. In figure 6.14 a plot of the mean of the cluster size in all the three DUTs in the telescope is shown, for each of the 5 energies investigated. The errors of the mean values were calculated by using the same equations specified in subsection 5.4.5, by first finding the standard deviation of each distribution and then calculating the standard error of the mean.

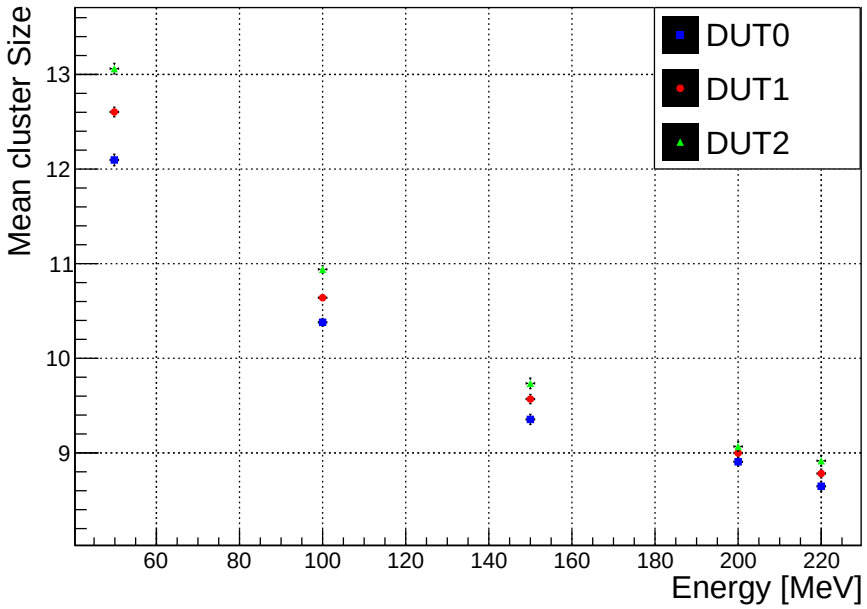

Figure 6.14: Cluser size vs energy for all the three chips from 50 MeV/n to 220 MeV/n. The blue, red and black points represent, respectively, the data for DUT0, DUT1, and DUT2.

For all the chips, the cluster size decreased with increasing helium energy. This result is as expected since the higher energy helium-ions deposits less energy in the chips resulting in a lower LET. As the energy decreases, the energy loss moves towards the Bragg peak, and the LET will, therefore, increase. In other words, the probability of creating larger clusters increases as the deposition energy increases and hence, the average cluster sizes are greater at lower energies than those at higher energies.

From the plots, it is also possible to observe how the cluster sizes increases as the particle crosses more silicon layers. This is, again, expected since the energy of the particle decreases as it moves through the telescope and will, therefore, deposit more and more energy in each successive layer. The cluster size differences of the three chips also decrease as the helium energy increases. This means that the LET increases more at each layer at lower energies, leading to the a larger energy deposition variance such that the mean of the cluster sizes for each successive layer have a wider spread.

Figure 6.14 does not show the actual cluster size at the different energies as doughnut-shape clusters were used, leading to a bias towards lower pixel numbers. The dependency, however, should be valid since the relative difference in the energy deposition should be the same. The mean cluster size of the chips decreased of roughly the same amount for each energy step and decreased in total 4 pixels going from 50 MeV/n to 220 MeV/n.

CHAPTER 7

Discussion and conclusion

The primary objective of this project was to characterize the ALPIDE chip by studying the cluster sizes produced by helium beams and a radioactive alpha source. The ALPIDE chip will operate as the tracking detector and the energy calorimeter in the future pCT system developed at the University of Bergen.

The main motivation of a pCT is to increase the range accuracy of proton treatment by eliminating the need for converting Hounsfield Units into Relative Stopping Power for the protons. The Relative Stopping Power can be calculated directly in a pCT scan by estimating the MLP of the proton inside the medium and measuring its remaining energy. The cluster sizes produced in the ALPIDE chips are used to enhance the energy measurement of protons inside the DTC by using the Bragg Curve fitting method. With this method, an estimation of the energy deposition of the particle in each layer is found using the number of firing pixels in each cluster. A Bragg Curve is fitted through these energy deposition points, and the energy is found by either looking at the stopping point of the curve and converting this range into energy or by integrating the curve.

The results from the experiment conducted at the ANSTO facility in Australia show that the cluster size does tend to change with the beam position. This indicates how the cluster size is correlated with the particle energy deposition on the pixel. At V_{bb}=0V , with a 10 MeV helium-ion scan, the cluster sizes varied from 5 to 35 pixels throughout a scan procedure which continuously changed the beam spot position, with a micrometer step.

An explanation of this phenomenon could be that the larger clusters are more likely to appear when a particle crosses the periphery of a pixel since the charge carriers are then generated further away from the n-diode. The opposite would then occur for particles crossing the middle of the pixels since the charge carriers would then be more likely to diffuse into the depletion region of the first n-diode. In other words, the charge concentration would decrease at a slower rate if the electron-hole pairs

were generated further away from a collecting n-diode and hence, they would be able to diffuse to more pixels.

If the cluster sizes vary w.r.t. the position of where the particle hit on the pixel, this would impact the Bragg curve fitting process in the DTC, as this method in its current state only uses the number of fired pixel to estimate the deposited energy. The Bragg curve fitting method, however, will most likely be improved in the future and would then be able to include this effect by, for example, using the path of each particle in the DTC to estimate the position of the deposited energy.

The results obtained from the threshold and noise scans showed that there were radiation-induced effects on the chip from the helium microbeam at ANSTO. These effects were relatively small, and would not likely have influenced the cluster sizes to the extent that was observed in the ANSTO data. The results from the temperature measurement done at the University of Bergen, however, showed that the mean of the cluster sizes increased by 2.75 pixels during a temperature variation from 15 to 40°C. As the chip at the ANSTO facility was located inside a vacuum chamber, and no conductive cooling of the chip was present. It is very likely that the heating of the chips contributed to increasing the cluster size, as an effect of the temperature raising.

The results from the HIT experiment on the ALPIDE telescope showed that there was a clear correlation between the helium beam energy and the produced clusters. As expected, the clusters increased in size as the beam energy decreased. The results also showed that there was a cluster size difference between each chip due to the LET increase of the helium particles within each layer. This is a good result regarding the future DTC, as it shows that the chips are able to separate different beam energies in relation to the cluster sizes.

Suggestions for future work:

i) Scan the ALPIDE chip in the x, y, and z directions to study its internal structure in 3D, and look at the relation between the position of the energy deposition and cluster size more accurately.

ii) Study the position of the deposited energy given by helium ions and protons by tracking and find the corresponding clusters. If a high precision tracking is possible, the energy deposition can be estimated both from the hit position of the particle on the pixel and the number of firing pixels.

iii) Study the ALPIDE response to helium and proton beams at clinical energies and intensities using a precise online monitoring system.

APPENDIX A

Acronyms

ALICE A Large Ion Collider Experiment

ALPIDE Alice Pixel Detector

ANSTO Australian Nuclear Science and Technology Organisation

CERN Conseil Europeen pour la Recherche Nucleairehev

CMOS Complementary Metal-Oxide-Semiconductor

CoG Center of Gravity

CT Computed Tomography

DAC Digital Analog Converter

DAQ Data Acquisition

DNA Deoxyribonucleic Acid

DTC Digital Tracking Calorimeter

DUT Device Under Test

HIT Heidelberg Ion Therapy Center

IB Inner Barrel

IMRT Intensity Modulated Radiation Therapy

ITS Inner Tracking System

LET Linear Energy Transfer

LHC Large Hadron Collider

MAPS Monolithic active pixel sensor

MIP Minimum Ionizing Particle

MRI Magnetic Resonance Imaging

PBRT Proton Beam Radiation Therapy

pCT Proton Computed Tomography

PET Positron Emission Tomography

RBE Relative Biological Effect

RSP Relative Stopping Power

TOT Time Over Threshold

APPENDIX B

Code example from the data processing

This code uses the event clock from the DAQ board to separate the events from the scanning procedure and to find the corresponding position of the beam. The average cluster size is then taken and plotted in a 128x128 matrix.

```
#include <iostream>
#include <fstream>
#include <string>
#include <vector>
#include <algorithm>
#include <TString.h>
#include <sstream>
#include <stdlib.h>
using namespace std;

int Hitmap() {

//Insert name of the file
const char* const files[] = {"Filename.txt"};

//Opens the file and reads in the data from the file
size_t sz = sizeof(files) / sizeof(files[0]);
std::ifstream fin;

//Creating the variables
for(size_t j = 0; j < sz; ++j) {
 int x, y, nhits = 0;
 double clocks, eventID = 0;
 std::vector <int> data_x = 0;
 std::vector <int> data_y = 0;
```

```
 std::vector <double> data_eventID = 0;
 std::vector <double> data_clocks = 0;
 std::vector <double> data_ClockDiff = 0;
 std::vector <double> data_eventIDDiff = 0;
 std::vector <int> data_nhits = 0;
 std::vector <int> data_interval = 0;
 std::vector <int> data_a = 0;
 std::vector <int> data_b = 0;
 std::vector <string> data_string = 0;
 double LineCounter = 0;
 int SmallCounter = 0;
 int DevideCounter = 0;
 string line;
 LineCounter = 0;
 SmallCounter = 0;
 DevideCounter = 1;
 double num = 0;
 int IDPresent = 0;
 int IDNext = 0;

// Reads in the file and finds the length
fin.open(files[j], std::ios_base::out);
while ( getline (fin,line) ){
 istringstream iss(line);
 do{
   string subs;
   iss >> subs;
   data_string.push_back(subs);
   SmallCounter++
   }
 while (iss);
 LineCounter++;
 }
fin.close();

//Taking the data into the 5 vectors
for(size_t i = 0; i < SmallCounter - 8; ++i) {
  if (DevideCounter == 1){
  num = atoi(data_string.at(i).c_str());
  IDPresent = atoi(data_string.at(i+2).c_str());
  IDNext = atoi(data_string.at(i+8).c_str());
```

```
 if (IDPresent == IDNext){
 i+= 5;
 continue;
 }

data_x.push_back(num);
DevideCounter++;
continue;
}

if (DevideCounter == 2){
num = atoi(data_string.at(i).c_str());
data_y.push_back(num);
DevideCounter++;
continue;
}

if (DevideCounter == 3){
num = atoi(data_string.at(i).c_str());
data_eventID.push_back(num);
DevideCounter++;
continue;
}

if (DevideCounter == 4){
num = atof(data_string.at(i).c_str());
data_clocks.push_back(num);
DevideCounter++;
continue;
}

if (DevideCounter == 5){
num = atoi(data_string.at(i).c_str());
data_nhits.push_back(num);
DevideCounter++;
continue;
}

if (DevideCounter == 6){
DevideCounter = 1;
continue;
```

```
  }
}


TH2F *hHitmap = new TH2F("hHitmap", "Average␣cluster␣size
   ␣w.r.t.␣beam␣position", 128,  0, 127, 128, 0,127);

//Setting the dwell time of the beam
double TimeEachInterval = 200;

char TimeConstant = TimeEachInterval;
double ClockInterval = ((TimeEachInterval*1000000)/12.5);
double ClockStart = data_clocks[0];
double ClockEnd = 0;
int IntNumber = 1;
int ToTIntNumber = 0;

//Estimating the beam position by using the event ID
   clock
for (int g = 0; g < data_x.size(); ++g) {
  ClockEnd = ClockStart + (IntNumber*ClockInterval);
   if (data_clocks[g] < (ClockEnd - 1000000000)){
   ClockEnd = ((ClockEnd + data_clocks[g]) - 4294967296);
   ClockStart = data_clocks[g];
   IntNumber = 1;
  }
  if (data_clocks[g] <= ClockEnd){
  data_interval.push_back(ToTIntNumber);
  continue;
  }
  else{
  IntNumber++;
  ToTIntNumber++;
  g += -1;
  continue;
 }
}

//Matching the clock ID to the spots
for(int h = 0; h < data_x.size(); h++){
 int a = (int) (data_interval[h] / 128);
 if (a % 2 == 0)   {
```

```
 int b = (data_interval[h] % 128);
  }
 else {
 int b = (127 - (data_interval[h] % 128));
 }
 data_a.push_back(a);
 data_b.push_back(b);
}

//Finding the average cluster size number
int SpotHit = 0;
int NumberSpot = 1;
int AverageHit = 0;

for(int v = 0; v < data_x.size(); v++){
  if(data_interval[v] > 16384){
  break;
  }
 SpotHit += data_nhits[v];
  if (data_interval[v] == data_interval[v+1]){
  NumberSpot ++;
  continue;
 }
  else{
  AverageHit = (SpotHit/NumberSpot);

//Filling the cluster sizes in the 128x128 matrix
  hHitmap->Fill(data_a[v], data_b[v], AverageHit);
  SpotHit = 0;
  NumberSpot = 1;
  AverageHit = 0;
  }
 }

hHitmap->Draw("COLZ");
}
return 0;
}
```

Bibliography

[1] N. Power. (2010) Interaction of gamma radiation with matter. [Online]. Available: https://www.nuclear-power.net/nuclear-power/reactor-physics/interaction-radiation-matter/interaction-gamma-radiation-matter/

[2] E. B. Podgorsak, *Radiation Physics for Medical Physicists*, D. of Medical Physics Centre universitaire de sante McGill University Health Centre Montreal Canada, Ed. Springer-Verlag Berlin Heidelberg, 2006.

[3] Kieranmaher. (2001) Basic physics of digital radiography. [Online]. Available: https://en.wikibooks.org/wiki/Basic_Physics_of_Digital_Radiography/The_Patient#/media/File:PhotoelectricEffect.jpg

[4] H. Pettersen, "A digital tracking calorimeter for proton computed tomography," Ph.D. dissertation, University of Bergen, 2018.

[5] L. Rossi and P. Fischer, *Pixel Detectors, From Fundamentals to Applications*. Springer-Verlag Berlin Heidelberg, 2006.

[6] O. Ametek, "Energy loss with heavy charged particles (alphas)," 2012.

[7] G. G. Milluzzo, "Monte carlo simulation and experimental tests of a faraday cup for absolute dosimetry with high pulsed ion beams," Ph.D. dissertation, Universita degli Studi di Catania, 2014.

[8] H. Paganetti, *Proton therapy physics*. Boca Raton: CRC Press, 2012.

[9] H. F. St. Olavs Hospital, "Idefaserapport regionale protonsentre," 2014.

[10] T. Bortfeld, "Imrt: a review and preview," *Department of Radiation Oncology, Massachusetts General Hospital and Harvard Medical*, 2006. [Online]. Available: stacks.iop.org/PMB/51/R363

[11] T. Mitin and A. Zietman, "Promise and pitfalls of heavy-particle therapy," *Journal of clinincal oncology*, 2014.

[12] N. B. Smith and A. Webb, *Introduction to Medical Imaging.* Cambridge University Press, 2011.

[13] R. Cierniak, *X-Ray Computed Tomography in Biomedical Engineering.* Springer, London, 2011.

[14] H. C. Berg, *Random Walks in Biology.* Princeton University Press, 1993.

[15] C. Honsberg and S. Bowden, "Diffusion," 2018. [Online]. Available: https://www.pveducation.org/pvcdrom/pn-junctions/diffusion

[16] W. Snoeys, "Cmos monolithic active pixel sensors for high energy physics," *Elsevier B.V*, 2014.

[17] V. N. Eikeland, "Characterization of the alpide detector for the development of a prototype proton computed tomography machine at the university of bergen," Master's thesis, University of Bergen, 2018.

[18] G. A. Rinella, "The alpide pixel sensor chip for the upgrade of the alice inner tracking system," *Elsevier B.V*, 2016.

[19] *EUTelescope*, http://eutelescope.web.cern.ch/, 2018.

[20] M. J. Berger and J. S. Coursey. (2017) Nist standard reference database 124. [Online]. Available: https://physics.nist.gov/PhysRefData/Star/Text/ASTAR.html

[21] O. Grottvik, "Design of high-speed digital readout system for use in proton computed tomography," Master's thesis, University of Bergen, 2007.

[22] R. Baskar, "Biological response of cancer cells to radiation treatment." *Frontiers in Molecular Biosciences*, 2004. [Online]. Available: https://www.ncbi.nlm.nih.gov/pmc/articles/PMC4429645/

[23] L. Gen and M. Suhag, "Radiotherapy : Basic concepts and recent advances," *MJAFI 2010; 66 : 158-162*, 2010. [Online]. Available: http://medind.nic.in/maa/t10/i2/maat10i2p158.pdf

[24] M. Mager, "Alpide, the monolithic active pixel sensor for the alice its upgrade," *Elsevier B.V*, 2015.

[25] D. team of Alice, "Alpide operations manual," 2016. [Online]. Available: http://www-subatech.in2p3.fr/~electro/projets/alice/dimuon/mft/pdf/ALPIDE-4-operations-manual_draft20160601.pdf

[26] S. Afroz, "Noise and cluster size studies of alpide-cmos pixel sensor for pct," Master's thesis, University of Bergen, 2018.